



Double-detonation Models for Type Ia Supernovae: Trigger of Detonation in Companion White Dwarfs and Signatures of Companions' Stripped-off Materials

Ataru Tanikawa^{1,2} , Ken'ichi Nomoto³ , Naohito Nakasato⁴ , and Keiichi Maeda⁵ 

¹ Department of Earth Science and Astronomy, College of Arts and Sciences, The University of Tokyo, 3-8-1 Komaba, Meguro-ku, Tokyo 153-8902, Japan
tanikawa@ea.c.u-tokyo.ac.jp

² RIKEN Center for Computational Science, 7-1-26 Minatojima-minami-machi, Chuo-ku, Kobe, Hyogo 650-0047, Japan

³ Kavli Institute for the Physics and Mathematics of the Universe (WPI), The University of Tokyo, 5-1-5, Kashiwanoha, Kashiwa, 277-8583, Japan

⁴ Department of Computer Science and Engineering, University of Aizu, Tsuruga Ikki-machi Aizu-Wakamatsu, Fukushima, 965-8580, Japan

⁵ Department of Astronomy, Kyoto University, Kitashirakawa-Oiwake-cho, Sakyo-ku, Kyoto 606-8502, Japan

Received 2019 May 23; revised 2019 September 18; accepted 2019 September 19; published 2019 November 5

Abstract

We have studied double-detonation explosions in double-degenerate (DD) systems with different companion white dwarfs (WDs) for modeling Type Ia supernovae (SNe Ia) by means of high-resolution smoothed particle hydrodynamics (SPH) simulations. We have found that only the primary WDs explode in some of the DD systems, while the explosions of the primary WDs induce the explosions of the companion WDs in the other DD systems. The former case is a so-called dynamically-driven double-degenerate double-detonation (D^6) explosion, or helium-ignited violent merger explosion. The SN ejecta of the primary WDs strip materials from the companion WDs, whose mass is $\sim 10^{-3} M_{\odot}$. The stripped materials contain carbon and oxygen when the companion WDs are carbon–oxygen (CO) WDs with He shells $\lesssim 0.04 M_{\odot}$. Since they contribute to low-velocity ejecta components as observationally inferred for iPTF14atg, D^6 explosions can be counterparts of subluminous SNe Ia. The stripped materials may contribute to low-velocity C seen in several SNe Ia. In the latter case, the companion WDs explode through He detonation if they are He WDs and through the double-detonation mechanism if they are CO WDs with He shells. We name these explosions “triple” and “quadruple” detonation (TD/QD) explosions after the number of detonations. The QD explosion may be counterparts of luminous SNe Ia, such as SN 1991T and SN 1999aa, since they yield a large amount of ^{56}Ni , and their He-detonation products contribute to the early emissions accompanying such luminous SNe Ia. On the other hand, the TD explosion may not yield a sufficient amount of ^{56}Ni to explain luminous SNe Ia.

Key words: binaries: close – galaxies: evolution – hydrodynamics – supernovae: general – white dwarfs

1. Introduction

Type Ia supernovae (SNe Ia) are one of the most luminous and common explosive objects in the universe and are utilized as a cosmic standard candle. However, their progenitors have been unclarified so far. Although it is widely accepted that an SN Ia is powered by a white dwarf (WD) explosion (Hoyle & Fowler 1960), the nature of its companion has been an open question. There are two popular scenarios on the companion types. The first is a nondegenerate star (main-sequence or red giant stars), the so-called single-degenerate (SD) scenario (Whelan & Iben 1973; Nomoto et al. 1984). The second possibility is another WD, namely the double-degenerate (DD) scenario (Iben & Tutukov 1984; Webbink 1984). The mass of an exploding WD has also been under debate; it can be near-Chandrasekhar-mass (Whelan & Iben 1973) or sub-Chandrasekhar-mass (Nomoto 1982).

Recent observations have imposed several constraints on the nature of their progenitors. It has been argued that the SD scenario may be disfavored for some SNe Ia. There are no red giant stars in the pre-explosion images of SN 2011fe and SN 2014J (Li et al. 2011; Kelly et al. 2014, respectively). A supernova remnant LMC SNR 0509-67.5 has no surviving main-sequence star (Schaefer & Pagnotta 2012; Litke et al. 2017). However, we note that spin-up/spin-down models can explain these nondetections (Di Stefano et al. 2011; Justham 2011; Hachisu et al. 2012; Benvenuto et al. 2015). On the other hand, a large amount of circumstellar materials (CSMs) have been indicated for PTF11kx (Dilday et al. 2012),

which supports the SD scenario. SNe Ia resulting from the He detonation (usually attributed for the sub-Chandrasekhar WDs) have been suggested, such as MUSSES1604D (Jiang et al. 2017) and ZTF18aaqeaq/SN 2018byg (De et al. 2019). X-ray observation with the *Hitomi* telescope has revealed that both near- and sub-Chandrasekhar-mass explosions are required to explain the abundance pattern of the iron-peak elements in the Perseus Cluster (Hitomi Collaboration et al. 2017). There is growing evidence that SNe Ia can have multiple progenitor channels (e.g., Hillebrandt et al. 2013; Maeda & Terada 2016).

It is then important to make clear the dominant progenitor of the standard candle and the origin of iron-peak elements. The dynamically-driven double-degenerate double-detonation (D^6) model (or helium-ignited violent merger model), one of the sub-Chandrasekhar-mass models in the DD scenario, can be a promising candidate as the dominant population of sub-Chandrasekhar-mass explosion. The discoveries of hypervelocity (HV) WDs (Shen et al. 2018a) have strongly advocated the D^6 model, since the D^6 model results in a WD thermonuclear explosion and an HV WD remnant. The thermonuclear explosion completely disrupts the primary WD. The companion WD suddenly becomes free from the gravity of the primary WD and is flung away at a hypervelocity as an HV WD. Although the current number of the confirmed HV WDs is too small for the D^6 model to explain all the SNe Ia, the observational sample may still be incomplete; an increasing number of HV WDs may be discovered in the future.

Table 1
Summary of Initial Conditions and Simulation Results

Model	M_p (M_\odot)	$M_{p,sh}$ (M_\odot)	$M_{p,He}$ (M_\odot)	M_c (M_\odot)	$M_{c,sh}$ (M_\odot)	$r_{sep,i}$ (10^4 km)	N (10^6)	Exp.	M_{ej} (M_\odot)	$M_{^{56}\text{Ni}}$ (M_\odot)	M_{Si} (M_\odot)	M_{O} (M_\odot)	M_{cos} (M_\odot)	E_{nuc} (Foe)	E_{kin} (Foe)
He45R09	1.0	0.05	0.03	0.45	...	2.9	60	TD	1.45	0.81	0.15	0.08	...	2.3	2.0
He45	1.0	0.05	0.03	0.45	...	3.2	60	D ⁶	0.98	0.56	0.15	0.07	0.0033	1.4	1.1
CO60He00	1.0	0.05	0.03	0.60	0.000	2.5	67	D ⁶	0.97	0.55	0.15	0.07	0.0028	1.4	1.1
CO60He06	1.0	0.05	0.03	0.60	0.006	2.5	67	D ⁶	0.97	0.54	0.15	0.07	0.0029	1.3	1.1
CO90He00	1.0	0.10	0.05	0.90	0.000	1.6	67	D ⁶	0.93	0.51	0.14	0.06	0.0024	1.4	1.1
CO90He09	1.0	0.10	0.05	0.90	0.009	1.6	80	D ⁶	0.94	0.52	0.14	0.06	0.0033	1.4	1.1
CO90He54	1.0	0.10	0.05	0.90	0.054	1.6	80	QD	1.90	1.01	0.28	0.16	...	2.5	2.1

Note. M_p and $M_{p,sh}$ are the masses of the primary and primary’s He shell, respectively, $M_{p,He}$ is the He mass in the primary’s He shell, and M_c and $M_{c,sh}$ are the masses of the companion and the companion’s He shell, respectively. $r_{sep,i}$ is the initial separation between the primary and companion. N is the number of the SPH particles used for each model. “Exp.” means the explosion mode. M_{ej} is the total mass of the SN ejecta. $M_{^{56}\text{Ni}}$, M_{Si} , and M_{O} are the masses of ⁵⁶Ni, Si, and O in the SN ejecta, respectively. M_{cos} is the mass of the companion-origin stream. E_{nuc} is the nuclear energy released by the explosion, and E_{kin} is the kinetic energy of the SN ejecta.

Since the D⁶ model needs small amounts of He materials so as to ignite He detonation by hydrodynamical effects, it leaves only a small amount of He-detonation products; it is consistent with properties of MUSSES1606D (Jiang et al. 2017; Maeda et al. 2018) and ZTF18aaqas/SN 2018byg (De et al. 2019).

The D⁶ model is more advantageous than other sub-Chandrasekhar-mass explosion models in various respects. In the Milky Way, the merger rate of DD systems with the super-Chandrasekhar-mass in total may be smaller than the SN Ia rate, although the total merger rate of DD systems is comparable to the SN Ia rate (Maoz et al. 2014, 2018). These arguments would support the D⁶ model, since for the D⁶ model DD systems do not necessarily exceed the Chandrasekhar mass in total. Note that other sub-Chandrasekhar-mass models, such as the violent merger model (Pakmor et al. 2010; Sato et al. 2015, 2016), spiral instability model (Kashyap et al. 2015, 2017), and detached DD model (Fenn et al. 2016), require DD systems with the super-Chandrasekhar mass in total. Collisional DD models can explode successfully even if their total mass is sub-Chandrasekhar-mass (Raskin et al. 2009; Rosswog et al. 2009; Lorén-Aguilar et al. 2010; Dong et al. 2015). However, the rate of such events has been unclear (Hamers et al. 2013; Toonen et al. 2018).

The discovery of the HV WDs has motivated us to examine the D⁶ model in detail. We aim at revealing the properties of the D⁶ model as astronomical transients. In Tanikawa et al. (2018, hereafter Paper I), we have reproduced the D⁶ explosion of a DD system by means of smoothed particle hydrodynamics (SPH) simulation coupled with nuclear reaction networks and have investigated properties of its SN ejecta and surviving WD. The main conclusions are summarized as follows: (1) The SN ejecta have a velocity shift, $\gtrsim 1000$ km s^{−1}, due to the binary motion of the exploding WD. (2) The SN ejecta contain low-velocity O components stripped from the companion WD, and the stripped O may be observed in nebular phase spectra. However, since the companion WD has no He shell, it was unclear whether the O components can be stripped from the companion WD when the companion WD has an outer He shell.

In this paper, we follow the D⁶ explosions for various DD systems. The D⁶ explosions have distinct features from the violent merger model, since they happen before the DD systems merge. Thus, the companion WDs can survive the explosions of the primary WDs. We focus on the interactions of the primary explosions with the companion WDs. In Paper I, we found that O components will be stripped from the

companion WD when the companion WD has no He shell. At this time, we assess whether the O components can be stripped from the companion WD even when the companion WD has an outer He shell. Moreover, we consider an He WD or a CO WD with an outer He shell as a companion WD and examine whether the companion WD also explodes. We should remark that Papish et al. (2015) have shown the explosion of the companion He WD, the so-called triple-detonation (TD) explosion. In addition to this explosion type, we find the explosion of the companion CO WD, which we call quadruple-detonation (QD) explosion. The TD/QD explosions will have common features with the collisional DD models, since both WDs explode in these models.

This paper is structured as follows. We present our method in Section 2. We show our results in Section 3. We discuss our results and summarize our paper in Sections 4 and 5, respectively.

2. Method

Our SPH code is the same as used in Paper I (see also Tanikawa et al. 2017; Tanikawa 2018a, 2018b). We adopt the Helmholtz equation of state (Timmes & Swesty 2000) for equation of state and the Aprox13 for nuclear reaction networks (Timmes et al. 2000). We parallelize our SPH code with the aid of the Framework for Developing Particle Simulator (Iwasawa et al. 2016) and vectorize particle–particle interactions by using the Advanced Vector eXtensions instructions explicitly (e.g., Tanikawa et al. 2012, 2013).

We summarize our initial conditions in Table 1. We prepare seven DD systems. Although all of them have super-Chandrasekhar-mass in total, sub- and super-Chandrasekhar systems should share some common properties in the D⁶ explosions. The relaxation method to make single and binary WDs is the same as in Paper I. Every DD system has a $1.0 M_\odot$ CO WD as its primary WD. Each of the primary WDs has a CO core and outer He shell. These DD systems have various companion WDs: two He WDs with $0.45 M_\odot$, two CO WDs with $0.60 M_\odot$, and three CO WDs with $0.90 M_\odot$. One of the $0.60 M_\odot$ CO WDs and two of the $0.90 M_\odot$ CO WDs have outer He shells. The model names are related to the total and He shell masses of the companion WDs. CO60He00 is identical to the DD system in Paper I. The DD systems have circular orbits. On these orbits except for He45R09, the Roche lobe radii of the companion WDs are the same as their radii (Eggleton 1983). The semimajor axis in He45R09 is 0.9 times that in He45.

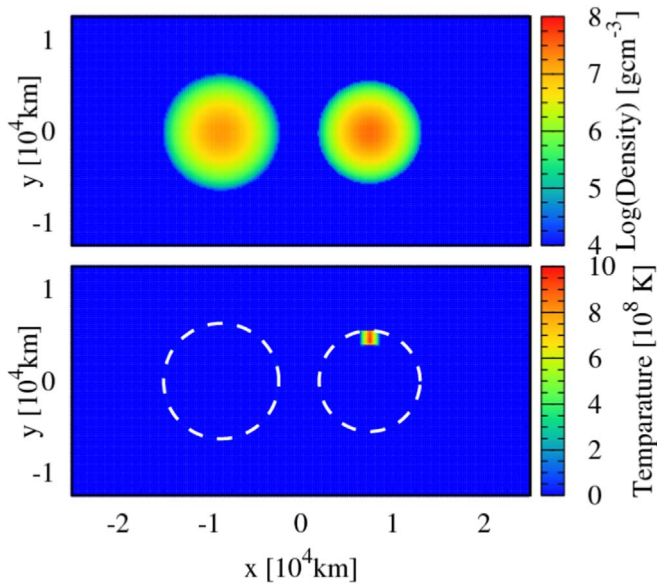


Figure 1. Initial density and temperature color maps on the orbital plane for CO90He00. These are slices, not projections, which is the same in the other figures. For the temperature color map, we delineate the primary and companion WDs by white dashed curves.

Although He45R09 should not appear in reality, we prepare this system for the following two reasons: (1) we determine the successful criteria of the TD explosion, and (2) we investigate the properties of the TD explosion that may succeed in a DD system with a realistic separation if its primary WD has a different mass from $1.0 M_{\odot}$.

The CO WDs (or their CO cores) consist of 50% C and 50% O by mass, and the He WDs consist of 100% He. For the primary WDs, their He shells are mixed with CO compositions composed of 50% C and 50% O by mass. The third and fourth columns indicate the total and He mass in the He shell of each primary WD, respectively. Thus, the He shells consist of 60% (50%) He, 20% (25%) C, and 20% (25%) O by mass for He45R09, He45, CO60He00, and CO60He06 (CO90He00, CO90He09, and CO90He54). For the companion WDs, the He shells have a pure He component.

Although the D^6 model can succeed even when the primary WD has a thin He shell (say, $0.01 M_{\odot}$), we set up the primary WDs in all the models with a thick He shell ($\sim 0.05 M_{\odot}$) in order to easily generate He and CO detonations in our SPH simulations. Therefore, we should be careful of chemical elements synthesized by He detonation. The primary WDs have their He shells consisting of He and CO compositions. The mixing also makes the initiation and propagation of He detonation easier (Shen & Moore 2014). The mixing can be achieved in DD systems in reality owing to Kelvin–Helmholtz instability in the merging process of DD systems (Pakmor et al. 2013). CO90He54 may have an unrealistically thick He shell (Iben & Tutukov 1985; Iben et al. 1987; Kawai et al. 1988; Iben & Tutukov 1991; Zenati et al. 2019). We set up this model to investigate features of the QD explosion.

As an example, we show the initial density and temperature color maps for CO90He00 in Figure 1. The center of mass of the DD system is located at the coordinate origin. The primary and companion WDs rotate counterclockwise around each other on the x - y plane. Thus, the orbital angular momentum points to the positive z -direction. In the primary WD, we set a hot spot large enough to generate an He detonation in the He

shell. The hot spot is at the x - y plane in the propagating direction of the primary WD, as seen in the bottom panel of Figure 1. We define the beginning of the He detonation as $t = 0$ s.

In all the models, an SPH particle has $m_{\text{SPH}} \sim 2.4 \times 10^{-8} M_{\odot}$. This corresponds to mass resolution with 4.2 million SPH particles per $0.1 M_{\odot}$. The total numbers of SPH particles are 60 million for He45R09 and He45, 67 million for CO60He00 and CO60He06, and 80 million for CO90He00, CO90He09, and CO90He54, summarized in Table 1. The SPH kernel length R , which is the effective space resolution, can be written as

$$R \sim \left(\frac{m_{\text{SPH}}}{\rho} \right)^{1/3} \sim 36 \left(\frac{\rho}{10^6 \text{ g cm}^{-3}} \right)^{-1/3} \text{ (km)}, \quad (1)$$

where ρ is the density. Note that the SPH kernel length (and the effective space resolution) in our SPH code becomes smaller for higher density.

Although our simulations have high-mass resolution with $\sim 10^{-8} M_{\odot}$, the resolution is not high enough to resolve detonation waves. Thus, we may highly simplify the initiation of detonation and detonation itself. In the Appendix, we compare detonations in our simulations with those in more realistic modelings.

In this paper, we use a polar coordinates system, as well as the Cartesian coordinates system, to draw figures. We adopt the ordinary way to transform the Cartesian coordinates system to the polar coordinates system.

3. Results

3.1. Overview

We summarize our simulation results and our initial conditions in Table 1. We can categorize the results of our DD systems into three explosion types: D^6 explosion, TD explosion, and QD explosion, as seen in the ‘‘Exp.’’ column. In the D^6 explosion, just the primary WD explodes as expected in the D^6 model. The D^6 explosions occur in He45, CO60He00, CO60He06, CO90He00, and CO90He09. On the other hand, both the primary and companion WDs explode in the cases of TD and QD explosions. DD systems in He45R09 and CO90He54 experience the TD and QD explosions, respectively. We describe in detail the D^6 , TD, and QD explosions in Sections 3.2, 3.3, and 3.4, respectively.

3.2. D^6 Explosions

Since we describe the D^6 explosion process in detail in Paper I, we briefly overview the explosion process here. In a DD system, Roche lobe overflow occurs from the lighter WD (companion WD) to the heavier WD (primary WD). When the primary or companion WD has an outer shell consisting of helium (He) materials, the He materials are ignited owing to hydrodynamical effects, and He detonation starts on the primary surface (Guillochon et al. 2010; Pakmor et al. 2013). The processes from the He detonation to carbon (C) ignition in the carbon–oxygen (CO) core are the same as the double-detonation mechanism. The He detonation does not ignite CO detonation in the CO core of the primary WD directly, differently from the classical double-detonation model (Nomoto 1982; Woosley et al. 1986). The He detonation surrounds the CO core. A shock wave separated from the He

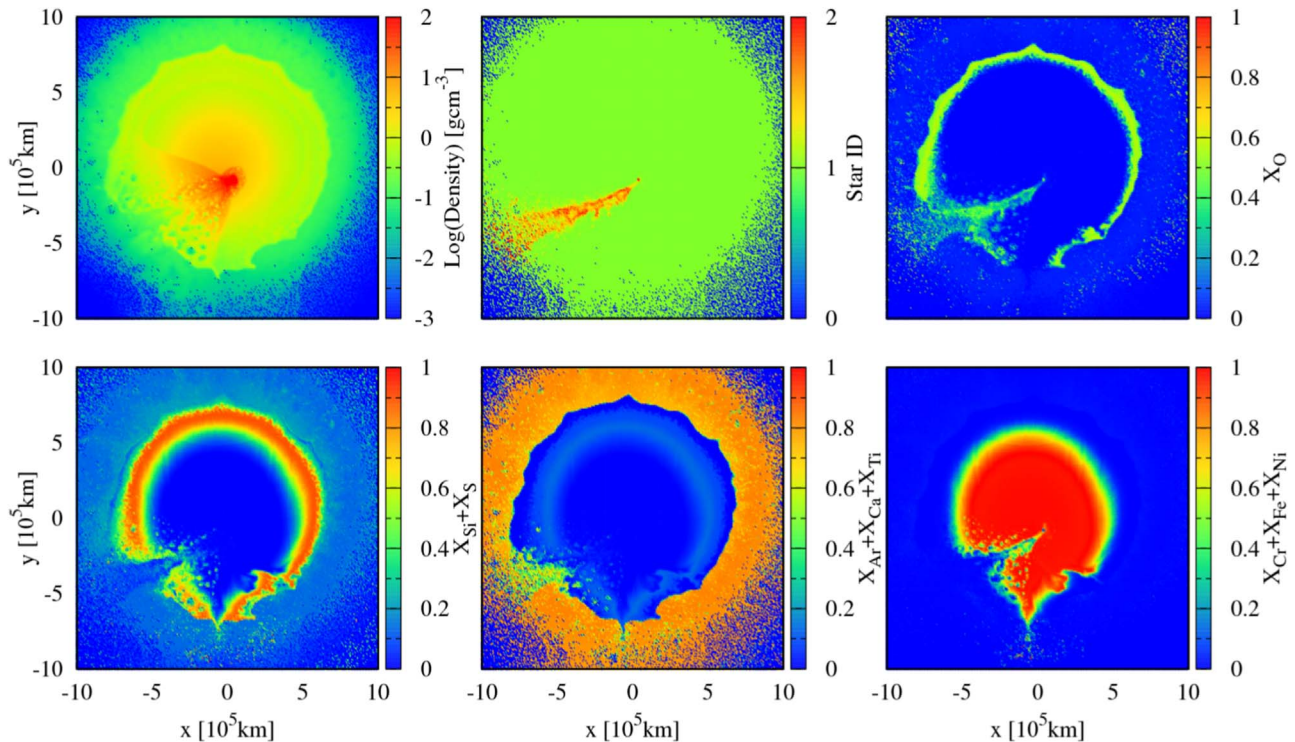


Figure 2. Density, star ID, and mass fraction of O, Si+S, Ar+Ca+Ti, and Cr+Fe+Ni at $t = 50$ s for CO90He00. The star ID indicates the origin of materials. When the star IDs of a material are 1 and 2, the material originates from the primary and companion WDs, respectively.

detonation invades into the CO core and converges at some point of the CO core. The convergence of the shock wave ignites C burning and generates CO detonation (Livne 1990; Livne & Glasner 1990). The CO detonation explodes the primary WD. The explosion generates a blast wave. The blast wave strips materials from the companion WD. The companion WD conversely acts as an obstacle against the blast wave and forms an ejecta shadow.

In Table 1, we see the masses of ejecta, ^{56}Ni , Si, and O for the D^6 explosions. The total ejecta mass is about $1.0 M_{\odot}$, which is the primary WD mass. However, it is slightly less than $1.0 M_{\odot}$. This is because small amounts of SN ejecta are captured by the companion WDs. The captured masses are $0.02 M_{\odot}$ for He45, $0.03 M_{\odot}$ for CO60He00 and CO60He06, and $0.06\text{--}0.07 M_{\odot}$ for CO90He00 and CO90He09. Shen & Schwab (2017) have analytically estimated that the captured masses are 0.006, 0.03, and $0.08 M_{\odot}$ for companion WDs with 0.3, 0.6, and $0.9 M_{\odot}$, respectively. Our results are in good agreement with the Shen & Schwab estimate.

The ^{56}Ni , Si, and O masses are similar among our D^6 models. As described in Paper I, these chemical abundances are consistent with the results of previous studies (e.g., Fink et al. 2010; Woosley & Kasen 2011).

We set thick He shells to generate He detonations easily. However, it has been discussed that the mass of the He shell could be smaller than the value adopted here, to initiate the He detonation. Indeed, such a scenario has been proposed for the D^6 explosion model to be consistent with properties of normal SNe Ia. The nucleosynthetic yields for such a thin He shell condition could be approximated by the results of the present model (thick He shell), as outlined below. First, He-detonation products are decreased. The He detonations in our simulations yield heavier Si group elements (argon, calcium, and titanium), not ^{56}Ni , since the He shells consist of mixture of He, C, and O.

Thus, the amount of heavier Si group elements is decreased by several $0.01 M_{\odot}$, and the amount of ^{56}Ni is unchanged. Next, CO-detonation products are increased. Since the He shells occupy low-density regions, the CO-detonation products should be products of C and O burnings, i.e., O and lighter Si group elements (silicon and sulfur). Consequently, the amount of O and lighter Si group elements is increased by several $\times 0.01 M_{\odot}$. In summary, O, Si, and S are increased by several $\times 0.01 M_{\odot}$ at the cost of the decrease of heavier Si group elements. These chemical abundances are still compatible with the results of the previous studies.

As an example, we show the SN ejecta at $t = 50$ s in CO90He00 in Figure 2. We can see an ejecta shadow (Papish et al. 2015) in the density color map. The color map of the star ID shows the presence of a companion-origin stream. The companion-origin stream consists of CO, as seen in the O color map, and does not contain He, since the companion WD has no He shell. Except for the ejecta shadow and companion-origin stream, the SN ejecta has a typical structure of the double-detonation explosion. Chemical elements are distributed in a spherical form and consist of ^{56}Ni , lighter Si group elements, O, and heavier Si group elements from inside to outside. The heavier Si group elements are yielded by the He detonation.

We investigate companion-origin streams. Figure 3 shows star IDs and mass fractions of He and O in CO60He00 and CO60He06 at $t = 50$ s. We can find from the left panels that both of the models have companion-origin streams. CO60He00, which has no He shell in the companion WD, does not contain He in their companion-origin streams, while CO60He06, which has an He shell in the companion WD, contains He in their companion-origin streams (see the middle panels). For CO60He06, its companion-origin stream also has O (see the right panels).

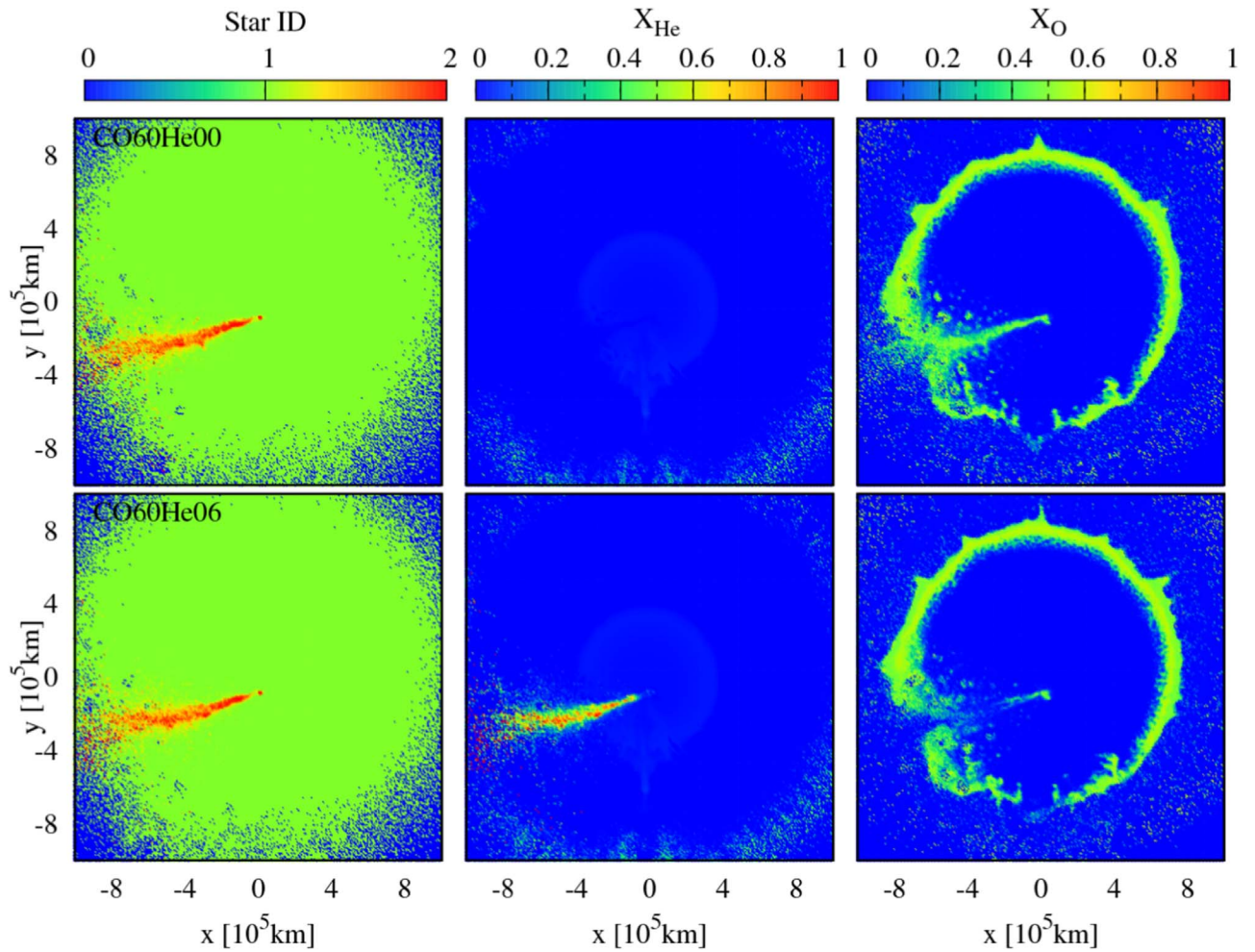


Figure 3. Star ID and mass fraction of He and O at $t = 50$ s for CO60He00 (top) and CO60He06 (bottom).

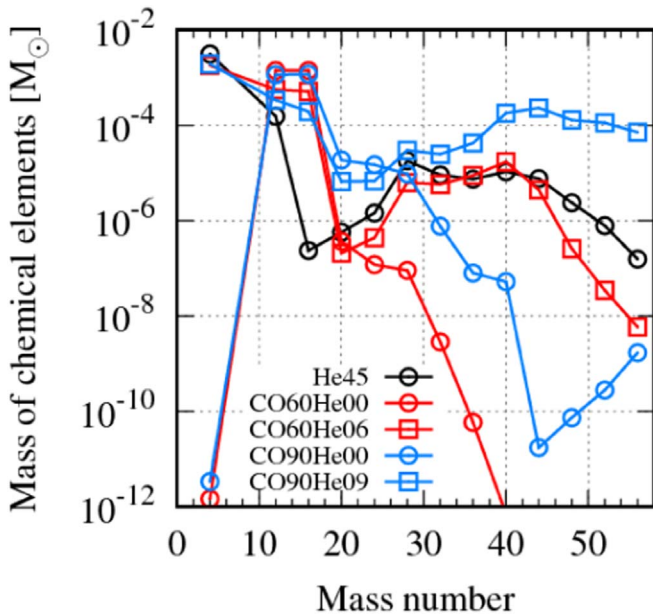


Figure 4. Chemical elements of companion-origin streams in He45, CO60He00, CO60He06, CO90He00, and CO90He09.

Figure 4 shows chemical elements of companion-origin streams in He45, CO60He00, CO60He06, CO90He00, and CO90He09. First, we describe properties of models with

CO WD companions. The He masses in CO60He00 and CO90He00 are much less than in CO60He06 and CO90He09. The latter models have the companion-origin streams with large amounts of unburned He. All the models have C+O in their companion-origin streams. Nevertheless, the C+O masses are decreased with increasing He shell masses. The masses of the lighter and heavier Si group elements are slightly larger in models with He shells than in models without He shells. He materials are burned by shock heating due to collision of SN ejecta with companion WDs.

Next, we investigate properties of He45. The chemical elements in the companion-origin stream are dominated by unburned He. Slight amounts of chemical elements other than He are present. These chemical elements are also formed by shock heating through collision of the SN ejecta with the companion WD.

The important point is that CO60He06 and CO90He09, as well as CO60He00 and CO90He00, include O materials in their companion-origin streams. In particular, the presence of O in CO60He06 (and also CO90He09) is unexpected for the following reason. Paper I (and Table 1) shows that the total mass of the companion-origin stream is $2.8 \times 10^{-3} M_{\odot}$ in CO60He00. Hence, if the outermost materials of CO60He06 are stripped, the companion-origin stream should consist of He only. We investigate the initial positions of materials in the companion-origin streams in CO60He06 and draw their initial

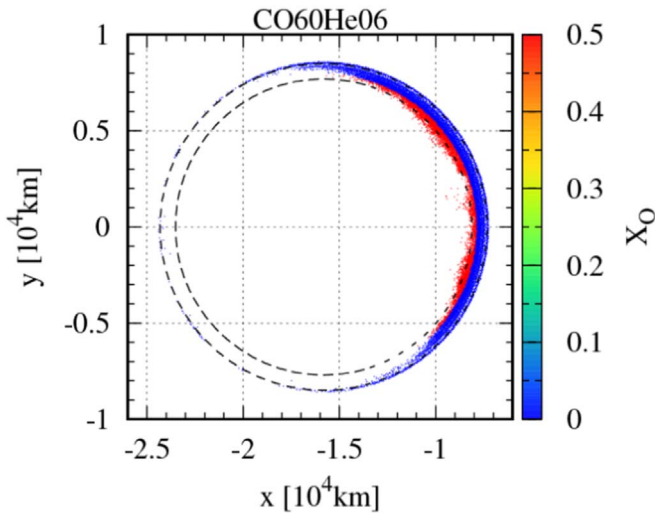


Figure 5. Initial position and oxygen mass fraction of stripped materials from the companion WD for CO60He06. We draw only materials with $|z| < 10^3$ km. The two dashed circles are used in Figure 6. They are centered at the center of the companion WD. The outer one indicates the surface of the companion WD, and the inner one can have any radii.

positions in Figure 5. This figure clearly shows that more materials are stripped on the nearer side of the primary WD, as shown analytically in Wheeler et al. (1975) and numerically in Hirai et al. (2014). Therefore, O can be stripped on the nearer side of the primary WD even if the companion WD has an He shell.

Figure 6 shows the depth of the stripped materials. As for models with companion CO WDs, we find that the depth distributions of stripped materials are nearly independent of the masses of He shells, comparing the depth between CO60He00 and CO60He06 and between CO90He00 and CO90He09. Slightly more materials are stripped with more massive He shells owing to He burning. The reason why the depth distribution in He45 is largely different from in other models would be the intensity of He burning.

Using Figure 6, we can conjecture the mass of O in a companion-origin stream when a companion CO WD has an He shell. A companion-origin stream contains $\sim 10^{-4}$, 10^{-5} , and $10^{-6} M_{\odot}$ of O, even if a companion WD has 0.013, 0.027, and $0.04 M_{\odot}$ of an He shell. When a companion WD has an He shell with more than $0.04 M_{\odot}$, the O mass is less than $10^{-6} M_{\odot}$ and dependent on the companion mass.

Figure 7 shows mass fractions of chemical elements as a function of radial velocity of SN ejecta from the viewing angle of $(\theta, \phi) = (90^{\circ}, 240^{\circ})$. From this viewing angle, features of companion-origin streams look most prominent. In all the models, the SN ejecta primarily have the heavier Si group elements, CO components, the lighter Si group elements, ^{56}Ni , and CO+He components from higher velocity to lower velocity. Except for the lower-velocity CO+He components, the distribution of the chemical elements is typical of the double-detonation explosion. The lower-velocity CO+He components come from the companion-origin streams. Although the lower-velocity CO+He components have less O with increasing He shell masses, low-velocity O components are still present. In the future, we should assess whether such low-velocity O components may be detected in the nebular phase of an SN Ia.

In Paper I, we found unburned materials due to numerical artifacts and converted them to ^{56}Ni . In this paper, we leave

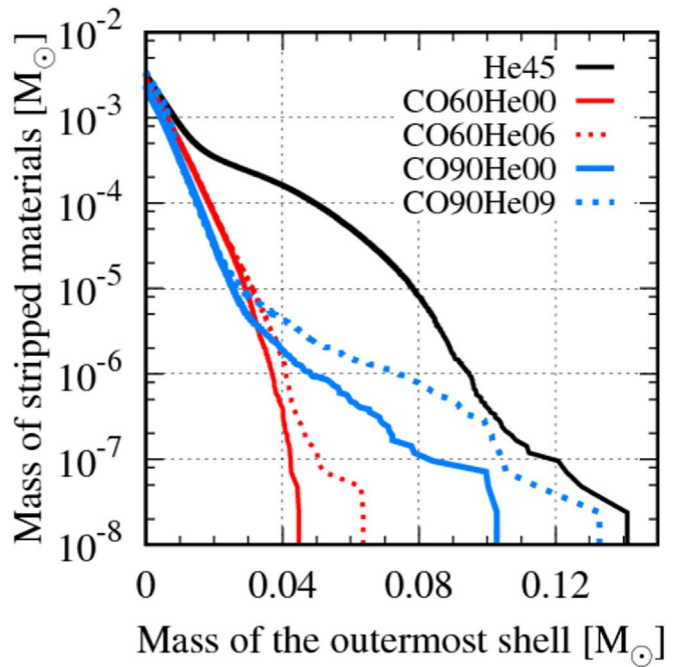


Figure 6. Mass of stripped materials inside of the inner dashed circle shown in Figure 5. The horizontal axis indicates the mass of a spherical shell between the two dashed circles in Figure 5. Note that the inner dashed circle can have any radii.

them as they are. They are captured by the companion WDs, and little is contained in the SN ejecta. Since they are initially located at the centers of the primary WDs, they get low velocities through the explosions of the primary WD. Eventually, they do not contaminate the SN ejecta.

3.3. TD Explosion

In this section, we describe properties of SN ejecta of a TD explosion that emerges in He45R09. Figure 8 draws the temperature evolution for He45R09. The processes are as follows. The CO detonation disrupts entirely the primary WD by $t = 2.50$ s. The resultant blast wave ignites an He detonation in the companion He WD just before $t = 3.50$ s. The He detonation disrupts the companion He WD by $t = 5.00$ s.

A TD explosion occurs in He45R09, while it does not in He45. The former binary separation is 2.9×10^4 km (or $0.041 R_{\odot}$), and the latter is 3.2×10^3 km (or $0.046 R_{\odot}$). This is quite consistent with the argument that a TD explosion is feasible if a binary separation is $\lesssim 0.045 R_{\odot}$ in Papish et al. (2015).

We should bear in mind that this DD system has an impractical configuration. Nevertheless, we investigate features of this explosion. This is because the TD explosion could occur if the primary WD has a different mass from $1.0 M_{\odot}$. For example, a DD system with 0.90 and $0.45 M_{\odot}$ WDs can be close to $\sim 0.045 R_{\odot}$.

We can see mushroom-shaped unburned regions at the center of the primary WD. We regard these unburned regions as numerical artifacts for the same reason as described in Paper I. We do not suspect that these unburned materials involve the beginning of the TD. As seen in the panel at $t = 3.50$ s, the TD explosion starts before these unburned materials hit the companion WD.

The total ejecta mass is $1.45 M_{\odot}$ (see Table 1), the same as the total mass of the DD system. It is larger than those in the D⁶

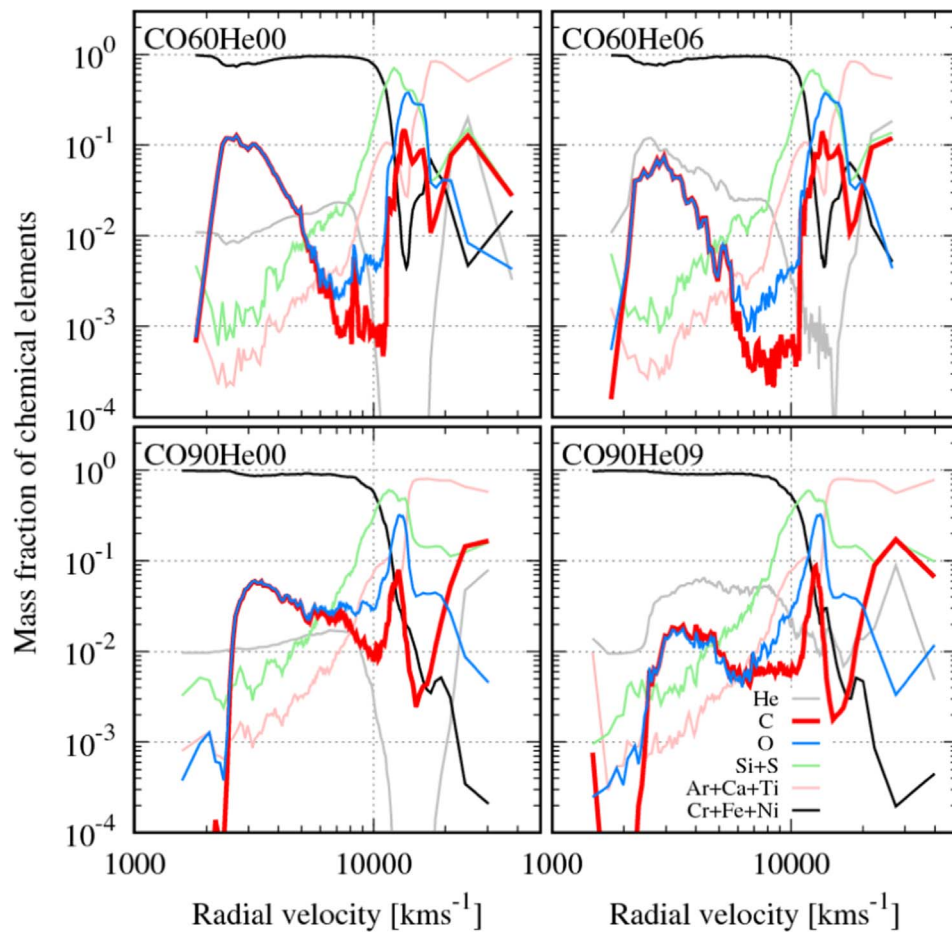


Figure 7. Mass fraction of chemical elements as a function of radial velocity at $t = 50$ s from the viewpoint of $(\theta, \phi) = (90^\circ, 240^\circ)$ for CO60He00, CO60He06, CO90He00, and CO90He09.

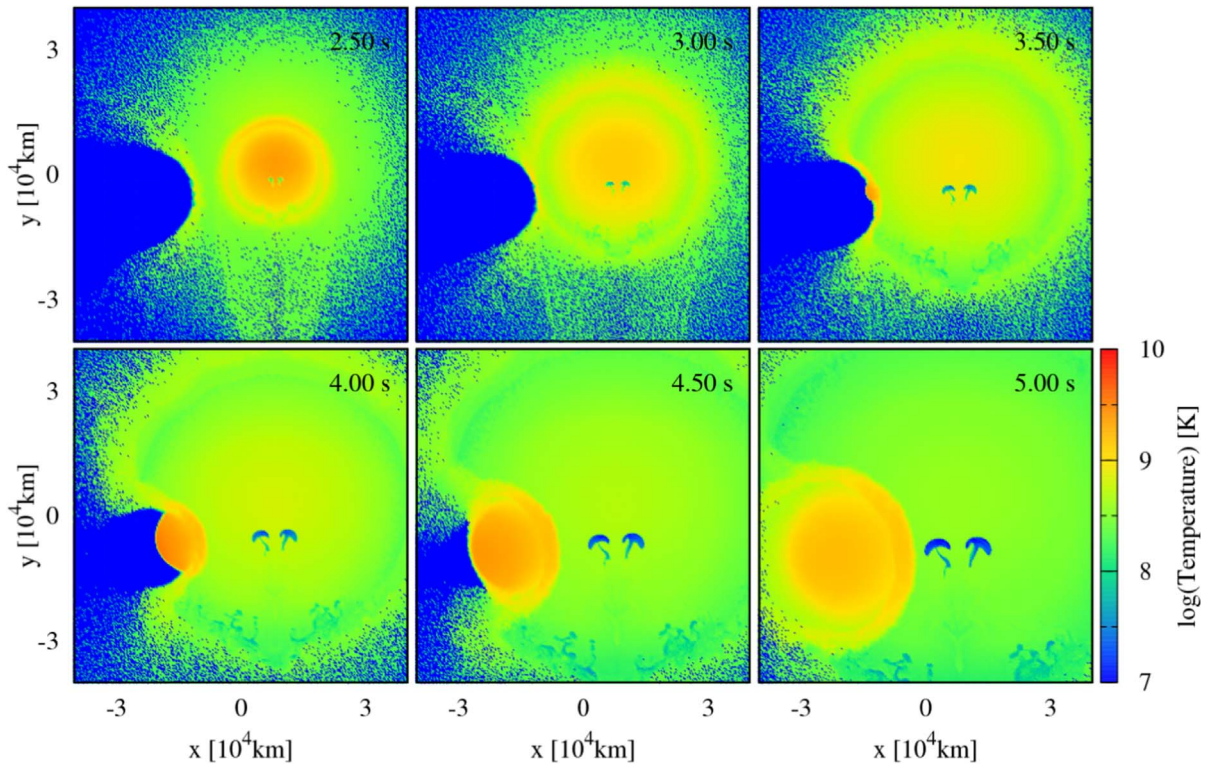


Figure 8. Temperature evolution for He45R09.

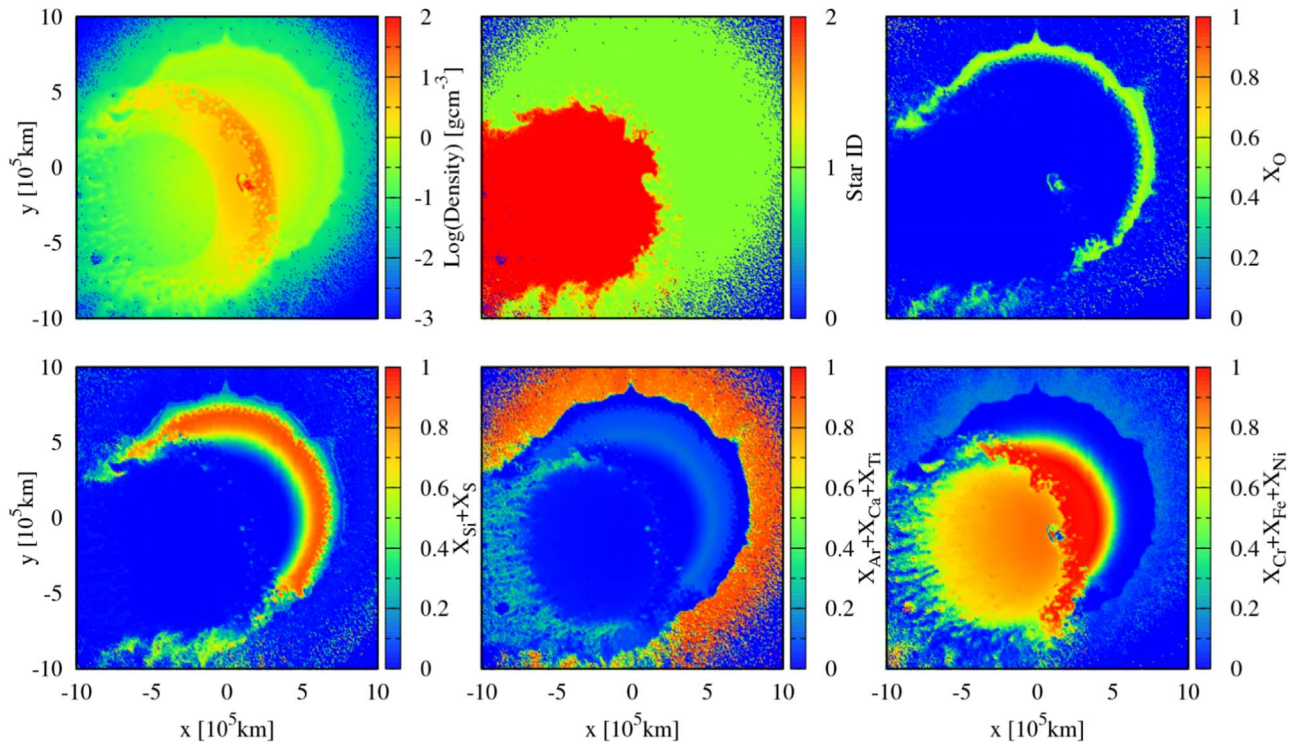


Figure 9. Same as Figure 2, except for He45R09.

explosion models by $\sim 0.5 M_{\odot}$. The increment of the ejecta mass consists of ^{56}Ni and He. The ^{56}Ni is the product of the He detonation in the companion WD. The Si, O, and C masses are similar to those in the D^6 explosion model.

Figure 9 shows SN ejecta in He45R09 at $t = 50$ s. The SN ejecta have overlapping structure of the two explosions. Since the companion WD explodes after the primary WD, the companion explosion overlays the primary explosion. The density color map indicates a crescent-shaped, high-density region. This region is formed through pushing back of the companion explosion against the primary explosion.

We show the mass fraction of chemical elements as a function of radial velocity at $t = 50$ s for He45R09 in Figure 10. From all the viewpoints, low-velocity components ($\lesssim 10^4$ km) consist mostly of ^{56}Ni and partly of He ($\sim 10\%$). These He materials are embers of the He detonation in the companion WD. From all the viewpoints but $(\theta, \phi) = (90^\circ, 180^\circ)$, high-velocity components ($\gtrsim 10^4$ km) are dominated by the lighter Si group elements, C+O, and the heavier Si group elements from lower velocity to higher velocity. This results from the primary’s explosion, a typical feature of double-detonation explosions. Chemical abundance seen from the viewpoint of $(\theta, \phi) = (90^\circ, 180^\circ)$ is completely different from those seen from the other viewpoints. Even in high-velocity components ($\gtrsim 10^4$ km), the dominant chemical elements are He and ^{56}Ni from lower velocity to higher velocity. This is because we see directly the companion’s explosion from this viewpoint.

3.4. QD Explosion

In this section, we show properties of SN ejecta of a QD explosion. First, we present processes of the QD explosion for CO90He54 in Figure 11. The CO detonation disrupts the primary WD by $t = 2.00$ s. The blast wave hits the companion

WD and generates the He detonation in the companion WD at $t = 2.25$ s. The He detonation surrounds the companion WD by $t = 3.75$ s and sends a converging shock wave into the companion WD. The converging shock ignites the CO detonation in the CO core of the companion WD at $t = 4.00$ s. The CO detonation explodes the companion WD by $t = 5.00$ s.

No QD explosion occurs in CO90He09. This is because the blast wave of the primary’s explosion completely strips the He shell of the companion WD on the near side of the primary WD before the blast wave ignites the He detonation.

Both the explosions of the primary and companion WDs leave unburned materials at their centers due to numerical artifacts. We do not expect these unburned materials to ignite the QD for the same reason as in the TD case. The unburned materials have not yet collided with the companion WD when the He and CO detonations in the companion WD start. When we investigate observational features of the QD, we have to be careful of the unburned materials from the companion WD. However, we need not be careful of the unburned materials from the primary WD. This is because the unburned materials in the primary WD are mixed with physically unburned materials in the companion WD owing to low density, and because the former mass is much smaller than the latter mass.

Figure 12 shows the SN ejecta at $t = 50$ s for CO90He54. The SN ejecta have a nested structure consisting of the explosions of the primary and companion WDs. As seen in the star ID panel, the outer and inner parts come from the primary and companion WDs, respectively, since the primary WD explodes before. The QD explosion has a nested structure, not an overlapping structure like the TD explosion. Since the QD explosion time is later than the TD explosion time (see Figures 8 and 11), the primary’s SN ejecta in the QD explosion have more time traveling farther away than in the TD explosion. From the outside to the inside, the SN ejecta have

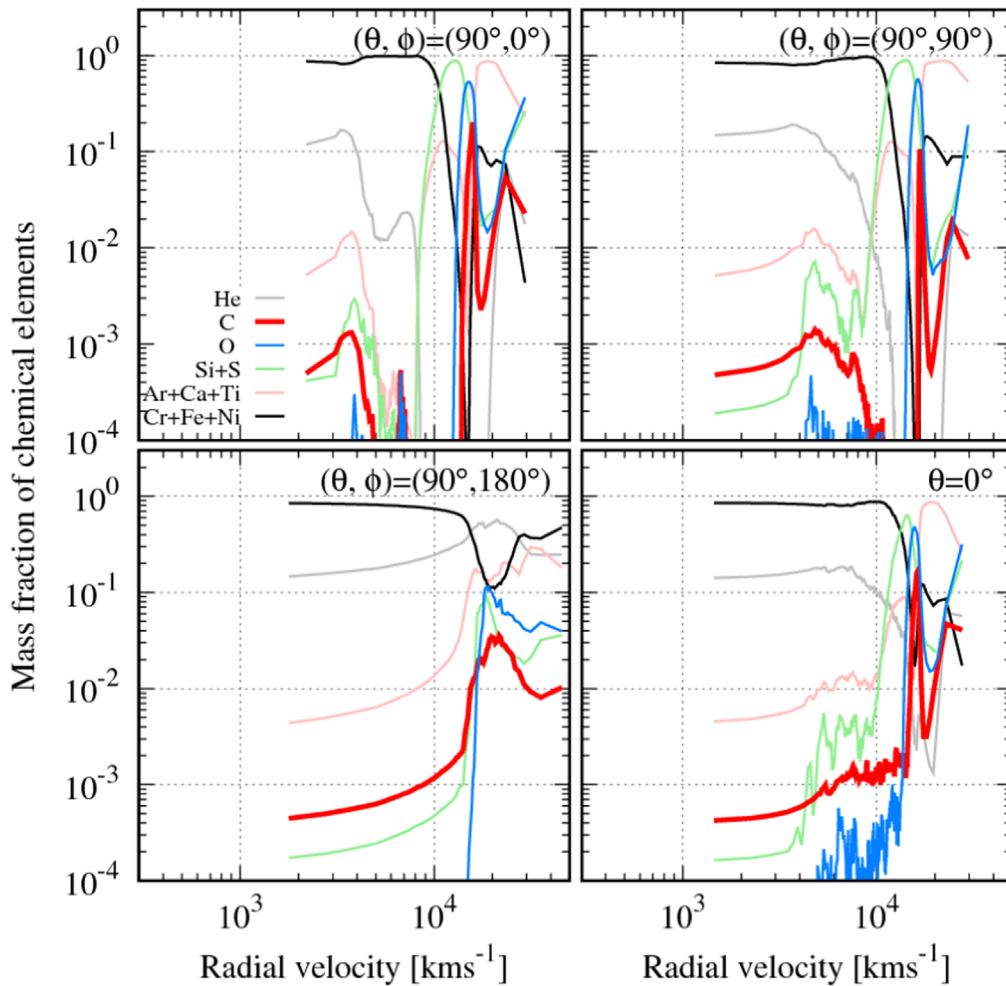


Figure 10. Mass fraction of chemical elements as a function of radial velocity at $t = 50$ s for He45R09. The viewpoint is indicated in the upper right corner of each panel.

the heavier Si group elements, O, the lighter Si group elements, ^{56}Ni , O, the lighter Si group elements, ^{56}Ni , and O. The heavier Si group elements in the outermost of the SN ejecta are synthesized by the He detonation in the primary WD. The outer ^{56}Ni elements are composed of those synthesized by the CO detonation in the primary WD and by the He detonation in the companion WD from the outside to the inside. The He detonation in the companion WD mainly yields ^{56}Ni , which is different from the He detonation in the primary WD. This is because the He shell of the companion WD consists of pure He.

The innermost part of the SN ejecta has O components, which are unburned materials due to numerical artifacts. The mass of these unburned materials is not large, $\sim 0.01 M_{\odot}$. However, we have to be careful that they contaminate chemical abundance in the inner part of the SN ejecta.

Figure 13 shows the chemical mass fractions as a function of radial velocity from various viewing angles. As expected, we can see the nested structure of the QD (two double-detonation) explosions. From higher velocity to lower velocity, the SN ejecta consist of He-detonation products, O, the lighter Si group elements, ^{56}Ni , O, the lighter Si group elements, and ^{56}Ni . In the panel with $(\theta, \phi) = (90^{\circ}, 180^{\circ})$, there are O components with $\sim 2000\text{--}3000 \text{ km s}^{-1}$, which come from unburned materials due to numerical artifacts.

4. Discussion

4.1. Counterparts of D^6 , TD, and QD Explosions

We discuss counterparts of D^6 , TD, and QD explosions. As described in Paper I, the D^6 explosion may be consistent with subluminescent SN Ia iPTF14atg. We will reproduce subluminescent SNe Ia if we choose masses of primary WDs to be less than $1.0 M_{\odot}$. Moreover, iPTF14atg has oxygen emission in its nebular phase (Kromer et al. 2016), which could be explained by a companion-origin stream in D^6 explosion. As shown in the previous section, a companion-origin stream can contain oxygen, even if a companion WD has an He shell. However, we note that the amount of oxygen is quite small. We should perform radiative transfer calculations in order to assess whether oxygen in a companion-origin stream can be detected in late-time spectra of SNe Ia.

Since the companion-origin stream also contains C, it may correspond to low-velocity ($\lesssim 10,000 \text{ km s}^{-1}$) C (Yamanaka et al. 2009; Folatelli et al. 2012; Silverman & Filippenko 2012; Cartier et al. 2014; Hsiao et al. 2015). Although C velocity is $\sim 3000 \text{ km s}^{-1}$ in Figure 7, the velocity may be $\sim 10,000 \text{ km s}^{-1}$ from different views. This is because the companion-origin stream spreads from the inner part of the SN ejecta to the outer part (see the right panels of Figure 4).

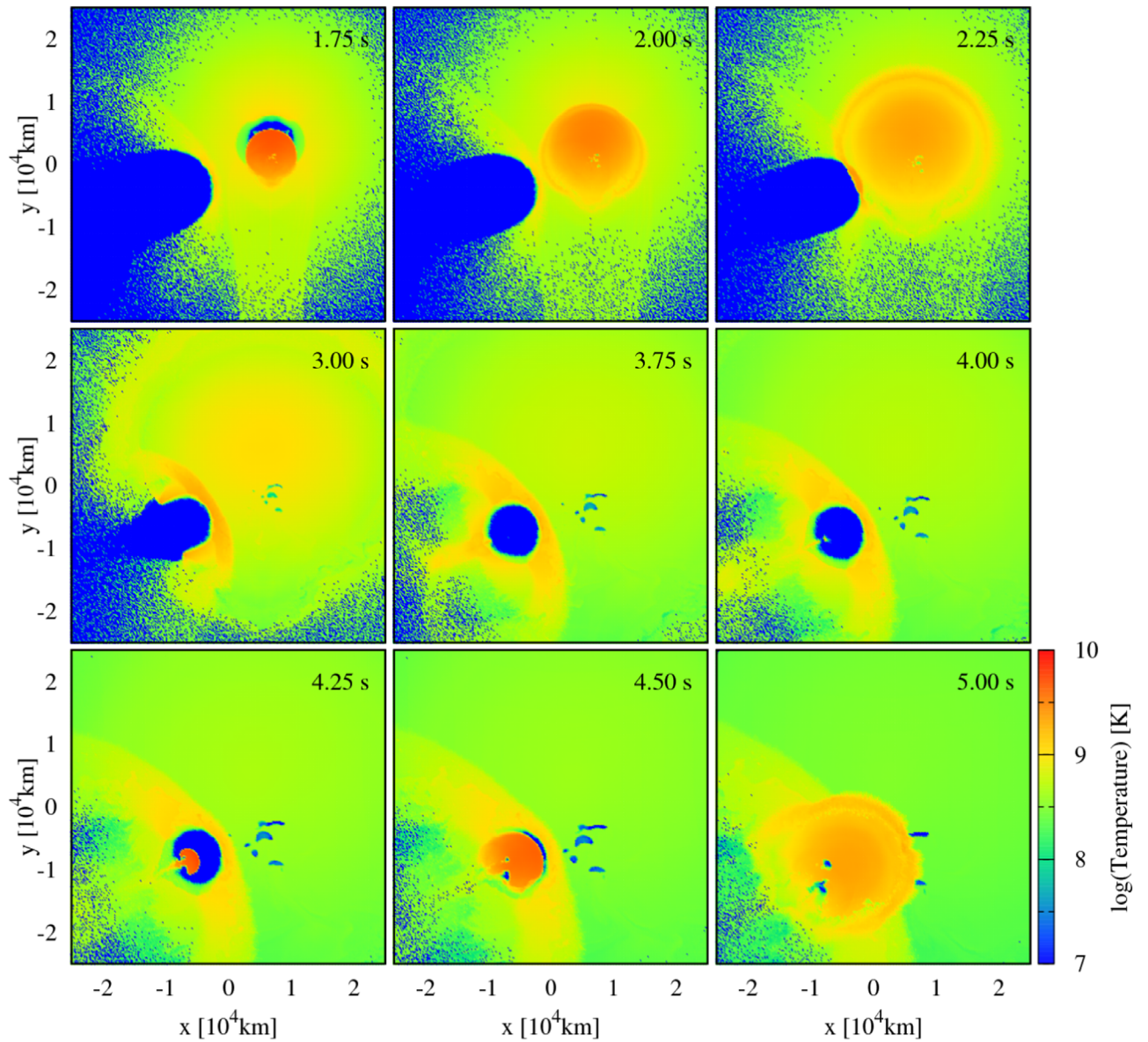


Figure 11. Temperature evolution for CO90He54.

Since TD and QD explosions yield a large amount of ^{56}Ni , we expect that their counterparts are super-Chandrasekhar SNe Ia or luminous SNe Ia, such as SN 1991T-like and SN 1999aa-like SNe Ia. However, we note that the TD explosion may not yield such a large amount of ^{56}Ni . The TD explosion may be achieved only when the primary WD has less than $1.0 M_{\odot}$ (more likely less than $0.9 M_{\odot}$). In this case, the primary WD yields $\sim 0.3 M_{\odot}$ of ^{56}Ni (e.g., Shen et al. 2018b). Then, the total ^{56}Ni mass should be $\lesssim 0.6 M_{\odot}$, which is not in agreement with those of luminous SNe Ia.

We thus discuss only the QD explosion. It may be difficult for the QD explosion to explain super-Chandrasekhar SNe Ia. Yamanaka et al. (2016) have reported that SN 2012dn, a candidate of super-Chandrasekhar SNe Ia, has massive CSMs. Such massive CSMs cannot be formed prior to the QD explosion.

We then discuss applicability of the QD explosion model to SN 1991T/1999aa-like SNe Ia. These luminous SNe Ia have been said to involve early excess optical/UV emission a few

days after their explosion (Jiang et al. 2018). This early excess emission could be consistent with surface ^{56}Ni formed by the He detonation on the primary or companion WD. Stritzinger et al. (2018) have shown that the early excess emission colors of luminous SNe Ia are relatively blue, $B - V \sim -0.1$. The He-detonation products can explain such a color (Maeda et al. 2018). Moreover, the He-detonation products can consistently make the UV emission of SN 1991T/1999aa-like SNe Ia, such as SN 2012cg and SN 2017cbv (Maeda et al. 2018), while interactions with a nondegenerate companion and CSMs may overproduce UV emission at the early phase (Hosseinzadeh et al. 2017; Maeda et al. 2018, respectively).

As seen in Figure 13, the QD explosion has high- and low-velocity components of ^{56}Ni . This may explain two-peak emission lines of Co III in SN 2007on (Dong et al. 2018). Note that Dong et al. (2018) have attributed such emission lines to the collisional DD models. Although SN 2007on is not luminous SNe Ia, such QD explosions can synthesize $< 0.6 M_{\odot}$ of ^{56}Ni mass if the primary and companion WDs have

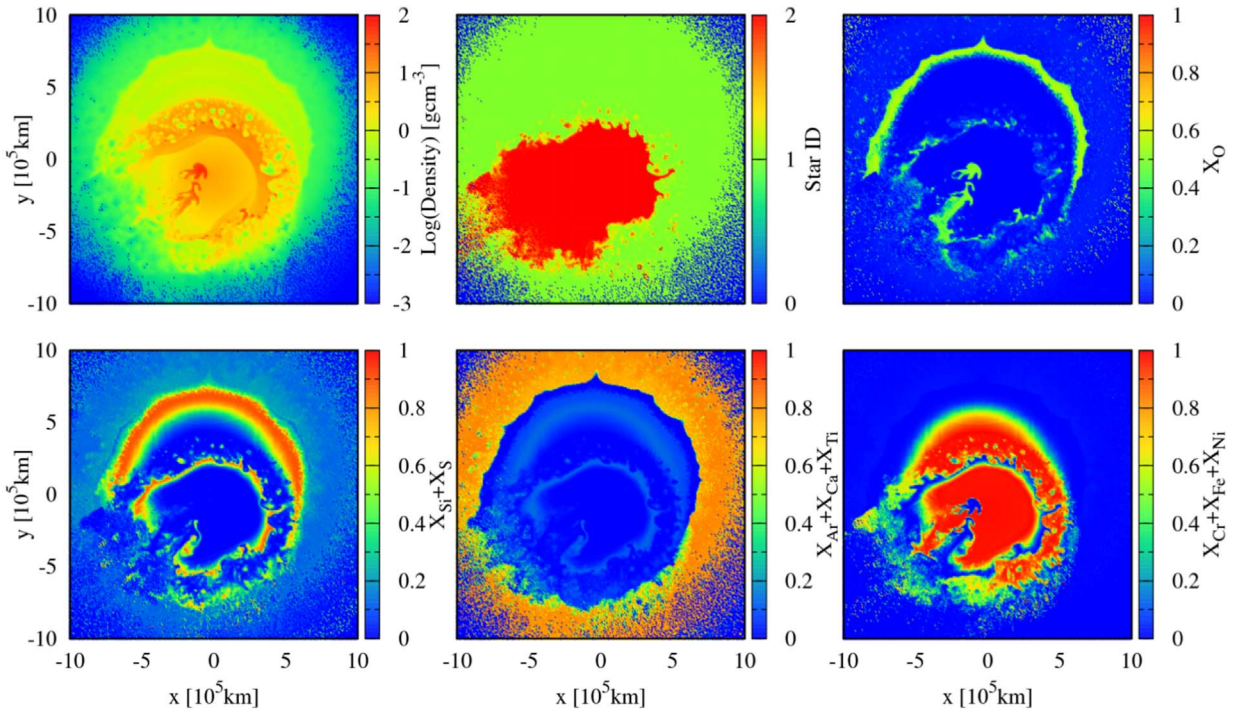


Figure 12. Same as in Figure 2, except for CO90He54.

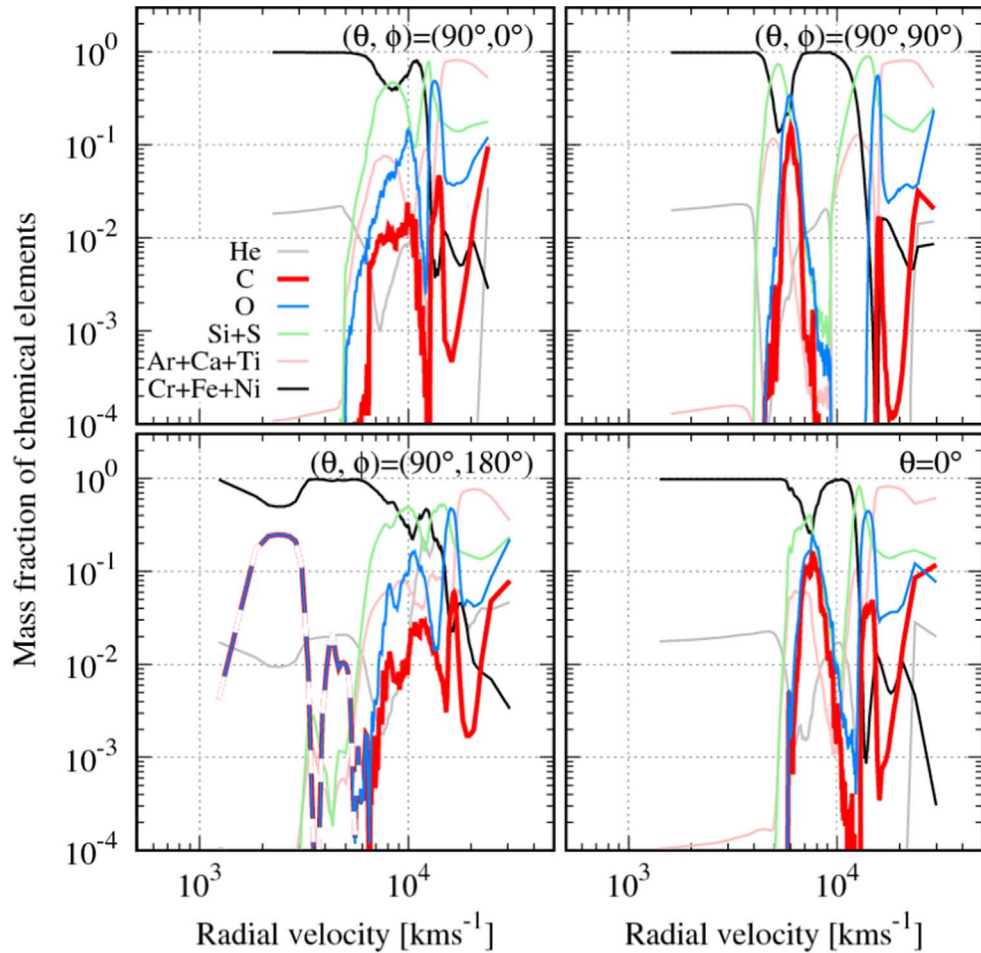


Figure 13. Same as Figure 10, except for CO90He54. In the panel of $(\theta, \phi) = (90^\circ, 180^\circ)$, low-velocity CO with $< 6 \times 10^3 \text{ km s}^{-1}$ is indicated by dashed curves, since these components come from unburned materials due to numerical artifacts.

$\lesssim 0.9 M_{\odot}$. However, the QD explosion may not make such prominent double-peak features of Co emission lines, since its ^{56}Ni distribution is nearly spherical, differently from ^{56}Ni distribution of the collisional DD models.

Finally, we mention a TD explosion. A TD explosion does not yield ^{56}Ni large enough to explain luminous SNe Ia. However, its spectra may be consistent with those of luminous SNe Ia, if it is observed from the side of the companion WD: $(\theta, \phi) = (90^{\circ}, 180^{\circ})$ in Figure 10. This is because Si emission lines cannot be observed from this side, which is consistent with luminous SNe Ia.

4.2. Comparison with Other Explosion Models

We compare D^6 , TD, and QD explosions with other sub-Chandrasekhar-mass explosions in DD systems, the violent merger model (Pakmor et al. 2010), the collisional DD model (Dong et al. 2015), the spiral instability model (Kashyap et al. 2015), and the detached DD model (Fenn et al. 2016).

We can distinguish D^6 explosions from the collisional DD model by oxygen emission lines in nebular phases. This model has no low-velocity oxygen. On the other hand, the violent merger and spiral instability models can have oxygen emission lines in the nebular phase (Taubenberger et al. 2013; Kromer et al. 2016; van Rossum et al. 2016). Thus, we should identify D^6 explosions from the violent merger and spiral instability models by velocity shift of SN ejecta of D^6 explosions (Paper I). This velocity shift comes from the binary motion of the exploding WD and is comparable to the velocity of an HV WD, $\sim 10^3 \text{ km s}^{-1}$. The difference between the D^6 and detached DD model should be whether He-detonation products are present or not.

We compare TD/QD explosions with the other DD models. The TD/QD explosions could leave He-detonation ashes. Thus, we can identify these explosions from the other DD models with footprints of He-detonation products. If these explosions can have double-peak features of Co emission lines in nebular phases, we can also differentiate these explosions from the violent merger, spiral instability, and detached DD models with the Co emission lines.

In addition, TD/QD explosions could be more luminous than these DD models, if the companion WD is massive. We compare their luminosities, assuming that their luminosities are proportional to the ^{56}Ni mass. TD and QD explosions yield 0.81 and $1.01 M_{\odot}$ of ^{56}Ni , respectively. On the other hand, the violent merger and spiral instability models yield $\sim 0.6 M_{\odot}$ of ^{56}Ni mass at most. ^{56}Ni mass of the collisional DD model is at most $0.4 M_{\odot}$. The detached DD model yields $0.86 M_{\odot}$ of ^{56}Ni . We find that the TD and QD explosions are at least 1.4 and 1.7 times more luminous than these DD models except the detached model, respectively. The QD explosion is still 1.2 times more luminous than the detached DD model, while the TD explosion is as luminous as the detached DD model. In summary, luminosity can be useful to identify the TD/QD explosions from the other DD models, except for the comparison between the TD explosion and detached DD model.

4.3. Detailed Nucleosynthesis

We derive detailed nucleosynthesis using simulation data by a post-processing method as follows. We pick up one SPH particle per 4096 SPH particles from three WDs: the

Table 2
Results of Detailed Nucleosynthesis

WDs	Fe (M_{\odot})	Mn/Fe	Ni/Fe
pWD in CO60He06	0.59	0.0025	0.057
cWD in He45R09	0.55	0.0031	0.053
cWD in CO90He54	0.21	0.0070	0.15

Note. The ‘‘pWD’’ and ‘‘cWD’’ indicate primary and companion WDs, respectively. The Mn/Fe and Ni/Fe show their mass fractions.

primary WD in CO60He06 as a representative of D^6 explosions, the companion WD in He45R09 (i.e., the companion WD of the TD explosion), and the companion WD in CO90He54 (i.e., the companion WD in the QD explosion). Thus, the number of SPH particles is 10,240 for the primary WD in CO60He06, 4608 for the companion WD in He45R09, and 9216 for the companion WD in CO90He54. We record density and temperature of these SPH particles every time step. Then, we calculate nucleosynthesis of these SPH particles by detailed nuclear reaction networks, using the torch code with 495 nuclei (Timmes 1999). We adopt the solar metallicity for the initial abundances of these SPH particles: 49.3% C, 49.3% O, and 1.3% ^{22}Ne in mass for SPH particles in CO cores, and 99% He and 1% ^{14}N in mass for SPH particles in He shells and He WDs.

We show stable nuclei of Fe, Mn, and Ni for comparison with the abundance pattern of 3C 397 in Table 2. Note that we do not take into account SPH particles in the He shells of the primary WD in CO60He06 and of the companion WD in CO90He54. We compare these results with previous studies (Yamaguchi et al. 2015; McWilliam et al. 2018; Shen et al. 2018b). As seen in the results of the $1.0 M_{\odot}$ CO WD (i.e., the primary WD of CO60He06), the mass fraction of Mn/Fe in our results is in good agreement with the previous results, while the mass fraction of Ni/Fe in our results is larger than in the previous results (~ 0.03). This may come from our simple modeling of detonations.

Although the mass fractions of Ni/Fe in our simulations are larger than those in previous studies, the mass fractions of Ni/Fe in D^6 , TD, and QD explosions are much less than that of 3C 397 ($\gtrsim 0.1$). The mass fraction of Ni/Fe in the companion WD of He45R09 is 0.15. However, the total mass fraction of Ni/Fe in the TD explosion is 0.081. The mass fraction of Mn/Fe is also much less than that of 3C 397 ($\gtrsim 0.02$). Thus, D^6 , TD, and QD explosions cannot explain the abundance pattern of 3C 397. The progenitor of 3C 397 may prefer a Chandrasekhar-mass explosion (Yamaguchi et al. 2015; Dave et al. 2017; Leung & Nomoto 2018).

4.4. Hypervelocity White Dwarfs (HV WDs)

D^6 explosions form HV WDs. Here, we consider the surface of HV WDs for HV WD observations. Just after the explosions, the surface materials consist of He, C, O, and ^{56}Ni when the companion WD is a CO WD. The C/O materials come from the HV WDs themselves. Since they are marginally stripped by the explosions of the primary WDs, they can be bound to the HV WDs. The ^{56}Ni materials are captured by the HV WDs from the SN ejecta. The He materials come from the primary WDs and He shells of HV WDs themselves. Note that the materials at the center of the primary WDs experience

α -rich freezeout. If the companion WD is an He WD, it has only He and ^{56}Ni on its surface.

It is not trivial that these chemical elements can be detected in HV WD observations. It should be clarified whether the captured ^{56}Ni materials and decay products stay on the surfaces of HV WDs. These ^{56}Ni materials and decay products may settle down into the inside of HV WDs after some time (Paquette et al. 1986; Dupuis et al. 1992) or may stay on the surface of HV WDs owing to radiative levitation (Chayer et al. 1995a, 1995b). The detection of these He materials depends on the surface temperature of HV WDs. Thus, we should follow the long-term evolutions of HV WDs in order to directly compare simulation results of HV WDs with HV WD observations. This is beyond the scope of this paper.

5. Summary

We have investigated nucleosynthesis signatures of stripping off and inducing detonation of companion WDs in double-detonation explosions for SNe Ia. We have found various explosion types of these systems: the D^6 , TD, and QD explosions. The D^6 explosions occur in the following conditions. The lighter WDs are CO WDs with thin He shells, or He WDs separated from the heavier WDs by $\gtrsim 0.045 R_\odot$. The D^6 explosions involve companion-origin streams. The companion-origin streams contain C+O even when the lighter WDs are CO WDs with He shells, $\lesssim 0.04 M_\odot$. These materials contribute to low-velocity components in SNe Ia. Thus, the D^6 explosions can be counterparts of subluminal SNe Ia, such as iPTF14atg. Moreover, the companion-origin stream may contribute to low-velocity C observed in several SNe Ia.

The QD explosion arises if the lighter WD has an He shell, $\gtrsim 0.05 M_\odot$. The QD explosion could be counterparts of luminous SNe Ia, such as SN 1991T and SN 1999aa, for the following two reasons: (1) the QD explosion yields large amounts of ^{56}Ni , $1.01 M_\odot$ for He90He54; and (2) it should accompany early emissions owing to the He-detonation products, whose colors may be consistent with the colors of SN 1991T-like and SN 1999aa-like SNe Ia, such as SN 2012cg and SN 2017cbv. If such QD explosions occur in DD systems with less massive CO WDs ($0.8\text{--}0.9 M_\odot$), they can be counterparts of SN 2007on with two-peak emission lines of Co III.

The TD explosion may be achieved only when the primary WD has less than $1.0 M_\odot$, say, $\lesssim 0.9 M_\odot$. Then, the TD explosion should yield $\lesssim 0.6 M_\odot$ of ^{56}Ni , which is not large enough to explain luminous SNe Ia. However, its spectra may be consistent with luminous SNe Ia, if it is observed from the side of the companion WD.

The D^6 explosions can be identified from other DD models by oxygen emission lines in the nebular phases, velocity shift, and signals of He-detonation products. The TD/QD explosions can be differentiated by their luminosities and signals of He-detonation products.

We thank Robert Fisher for fruitful advice. Numerical computations were carried out on Oakforest-PACS at the Joint Center for Advanced High Performance Computing and on Cray XC50 at the Center for Computational Astrophysics, National Astronomical Observatory of Japan. The software used in this work was in part developed by the DOE NNSA-ASC OASCR Flash Center at the University of Chicago. This research has been supported by the World Premier International

Research Center Initiative (WPI Initiative), MEXT, Japan; by the Endowed Research Unit (Dark side of the universe) by Hamamatsu Photonics K.K.; by the MEXT program for the Development and Improvement for the Next Generation Ultra High-Speed Computer System under its Subsidies for Operating the Specific Advanced Large Research Facilities; by the ‘‘Joint Usage/Research Center for Interdisciplinary Large-scale Information Infrastructures’’ and ‘‘High Performance Computing Infrastructure’’ in Japan (Project ID: jh180021-NAJ, jh190021-NAJ); and by Grants-in-Aid for Scientific Research (16K17656, 17K05382, 17H02864, 17H06360, 18H04585, 18H05223, 19K03907) from the Japan Society for the Promotion of Science.

Software: Modules of Helmholtz EOS and Aprox13 in FLASH (Fryxell et al. 2000, 2010), torch (Timmes 1999).

Appendix A

In our simulations, we may highly simplify initiation and propagation of detonations. In order to assess the simplifications, we compare detonations in our simulations with those in more realistic modelings. We investigate five detonations: He and CO detonations in the primary WD of CO60He00 as representatives of those in the primary WDs of all the models, He detonation in the companion WD of He45R09 (i.e., the third detonation in the TD explosion), and He and CO detonations in the companion WD of CO90He54 (i.e., the third and fourth detonations in the QD explosion, respectively).

In order to investigate detonations, we obtain physical quantities at grid points we put optimally for each detonation. We use an SPH interpolation to obtain these quantities, such that

$$q_i = \sum_j m_j \frac{q_j}{\rho_j} W(|\mathbf{r}_i - \mathbf{r}_j|, h_j), \quad (2)$$

where the subscripts i and j indicate quantities of a grid point and an SPH particle, respectively, and q , m , ρ , \mathbf{r} , h are general quantity, mass, density, position vector, and kernel-support length, respectively. We adopt the C^2 Wendland function for the SPH kernel function W (Wendland 1995; Dehnen & Aly 2012) in the same way as our simulations. The C^2 Wendland function in 3D is expressed as

$$W(r, h) = \frac{1}{h^3} (1 - \hat{r})_+^4 (1 + 4\hat{r}), \quad (3)$$

where $\hat{r} = r/h$, and $(\cdot)_+ = \max(0, \cdot)$.

We put 1024 uniformly spaced grid points along lines or curves for investigating detonations (see Figure 14). These lines and curves can be expressed as

$$\begin{aligned} \mathbf{r} &= \mathbf{r}_p + R_p (\cos(s/R_p + \pi/2) \sin(s/R_p + \pi/2), 0) \\ &\times (0 \leq s \leq \pi R_p) \end{aligned} \quad (4)$$

$$\mathbf{r} = \mathbf{r}_c + s (\cos(9\pi/8), \sin(9\pi/8), 0) \quad (-L \leq s \leq L) \quad (5)$$

$$\begin{aligned} \mathbf{r} &= \mathbf{r}_c + R_c (\cos(s/R_c), \sin(s/R_c), 0) \quad (0 \leq s \leq 4\pi R_c/3) \\ & \quad (6) \end{aligned}$$

$$\mathbf{r} = \mathbf{r}_p + s(0, 1, 0) \quad (-L \leq s \leq L) \quad (7)$$

$$\mathbf{r} = \mathbf{r}_c + s (\cos(5\pi/36), \sin(5\pi/36), 0) \quad (-L \leq s \leq L) \quad (8)$$

for He detonation in the primary WD of CO60He00, He detonation in the companion WD of He45R09, He detonation in the companion WD of CO90He54, CO detonation in the primary WD of CO60He00, and CO detonation in the companion WD of

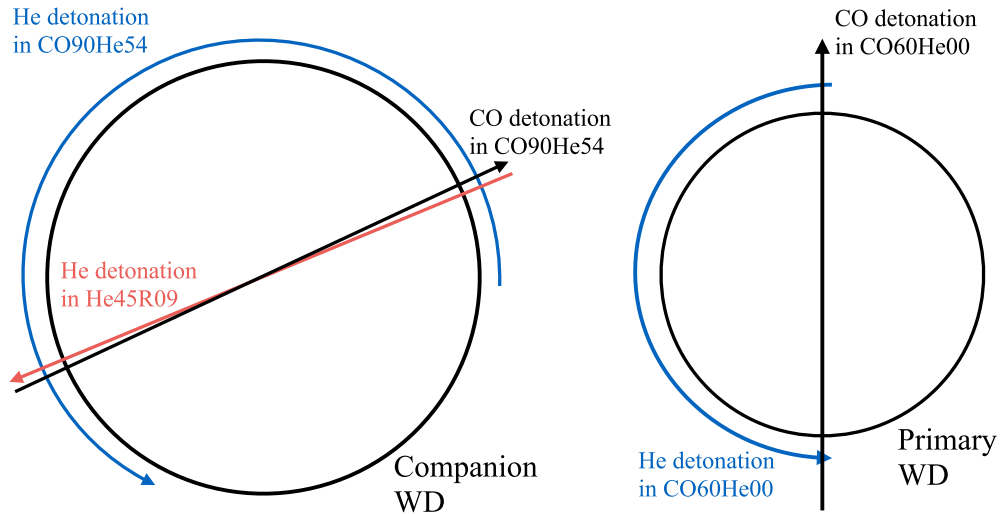


Figure 14. Lines and curves on which we put grid points in order to investigate the initiation and propagation of detonations. The detail definitions are described in Equations (4)–(8).

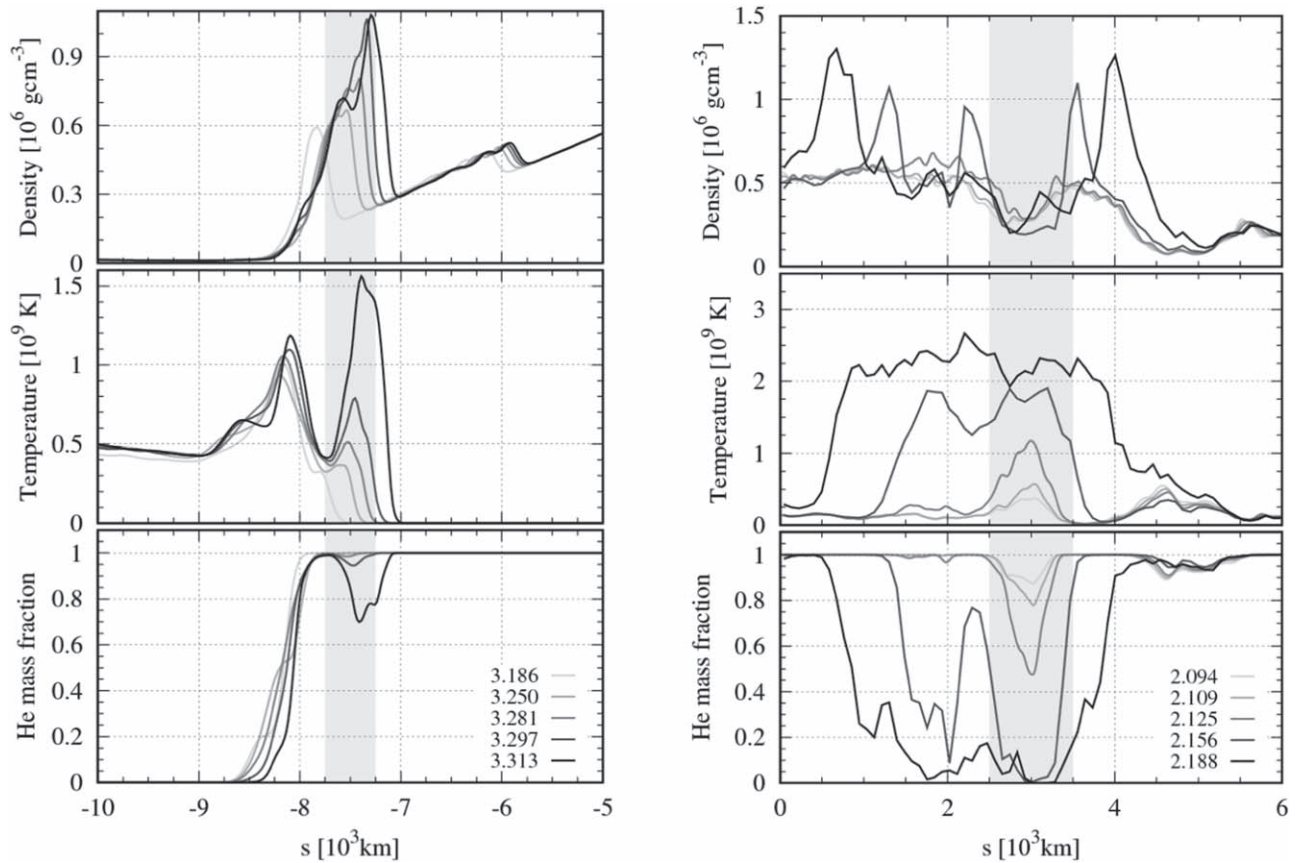


Figure 15. Formation of hot spots of He detonations in the companion WDs of He45R09 (left) and CO90He54 (right). The time is from $t = 3.186$ to 3.313 s (left) and from $t = 2.094$ to 2.188 s (right). The hot spot regions are indicated by shaded areas.

CO90He54, respectively. Here s is the coordinate along the line or curve and is used for the horizontal axes of Figures 15–20. r_p and r_c are the position vectors of the centers of the primary and companion WDs, respectively. R_p and R_c are approximately the radii at the bases of He shells of the primary and companion WDs, respectively, where $R_p = 4.6 \times 10^3$ km and $R_c = 5.5 \times 10^3$ km. Finally, $L = 10^4$ km.

In Appendices A and B, we show the initiation and propagation of detonations, respectively.

Appendix A.1 Initiation of Detonation

In this appendix we confirm that we do not overproduce detonations. We refer to Holcomb et al. (2013; H13) and Seitenzahl et al. (2009; S09) as sufficient conditions of initiation of He and CO detonations, respectively. We present He detonations first and CO detonations next.

The He detonation in CO60He00 starts from a hot spot we put artificially. The hot spot has a density of $\sim 10^6$ g cm $^{-3}$,

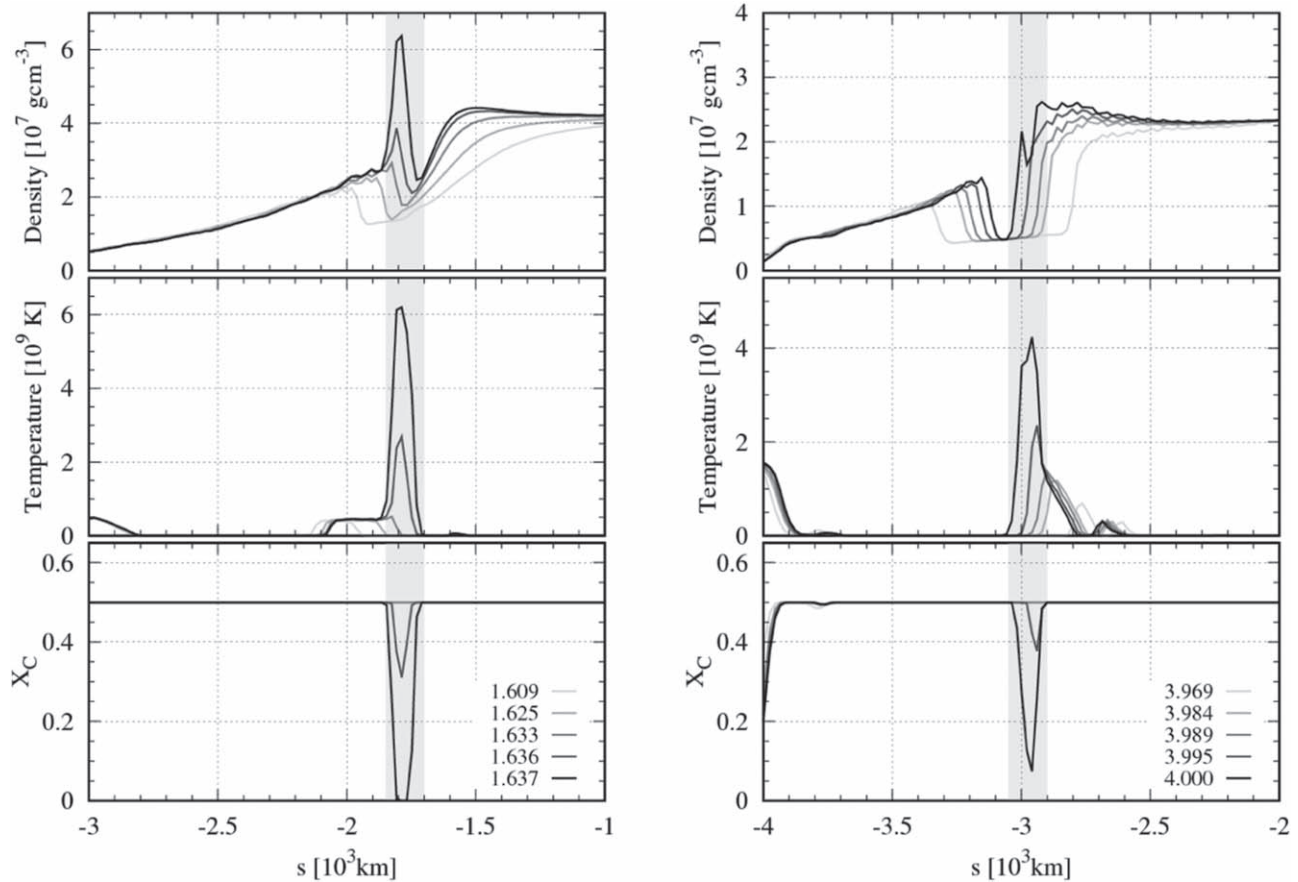


Figure 16. Formation of hot spots of CO detonations in the primary WD of CO60He00 (left) and in the companion WD of CO90He54 (right). The time is from $t = 1.609$ to 1.637 s (left) and from $t = 3.969$ to 4.000 s (right). The hot spot regions are indicated by shaded areas.

Table 3
Hot Spot Sizes and Space Resolutions at the Hot Spots

Model	CO06He00 (He)	He45R09 (He)	CO90He54 (He)	CO60He00 (CO)	CO90He54 (CO)
Size (km)	$\sim 10^3$	$\sim 10^3$	$\sim 10^3$	$\sim 10^2$	$\sim 10^2$
Resolution (km)	36	36	45	13	13

Note. The first line indicates model names and detonation types.

temperature of $\sim 10^9$ K, and size of $\sim 10^3$ km (see, e.g., Figure 1). As for H13, such a hot spot can start He detonation. Thus, we do not overproduce He detonation in CO60He00. This is the same for the other models undergoing D^6 and TD/QD explosions.

Figure 15 shows the formation of hot spots of He detonations in the companion WDs of He45R09 and CO90He54 as seen in temperature evolution. The definition of s in the horizontal axis can be found in Equations (5) and (6) for the left and right panels, respectively.

We first explain properties of the hot spot of the He detonation in the companion WD of He45R09. We can see that the He mass fraction drastically changes at $s \sim -8 \times 10^3$ km, such that the He mass fraction is zero at $s \lesssim -8.5 \times 10^3$ km and unity at $s \gtrsim -7.75 \times 10^3$ km. Thus, the surface of the companion WD is at $s \sim -8 \times 10^3$ km. Materials consist of SN ejecta at $s \lesssim -8 \times 10^3$ km and the companion WD at $s \gtrsim -8 \times 10^3$ km. This is why the temperature at $s \lesssim -8 \times 10^3$ km is high ($\gtrsim 5 \times 10^8$ K). There is a high-temperature ($\sim 10^9$ K) region at $s \sim -8 \times 10^3$ km. At this

region, the SN ejecta collide with the companion WD. The hot spot appears not at the center of the high-temperature region but at the skirt of this region inward of the companion WD at $s \sim -7.5 \times 10^3$ km. This may be because the center of the high-temperature region has low density, $\lesssim 10^5$ g cm $^{-3}$. The hot spot has a density of $\sim 10^6$ g cm $^{-3}$ and size of $\sim 10^3$ km. At that density, a hot spot with a size of $\sim 10^2$ km can be large enough to ignite He detonation.

We next see the hot spot of the He detonation in the companion WD of CO90He45. The hot spot appears at $s \sim 3 \times 10^3$ km. This is the nearest side of the companion WD from the primary WD. The hot spot has a density of 3×10^5 g cm $^{-3}$ and size of $\sim 10^3$ km. This hot spot is also sufficiently large for He detonation.

These hot spots are well resolved in our simulations. We can calculate effective space resolution of our simulations at these hot spots, using Equation (1) in Section 2. In these densities, the space resolutions are ~ 36 km for the former ($\sim 10^6$ g cm $^{-3}$) and ~ 45 km for the latter ($\sim 5 \times 10^5$ g cm $^{-3}$). These results are summarized in Table 3.

Figure 16 shows the formation of hot spots of CO detonations in the primary WD of CO60He00 and in the companion WD of CO90He54 as seen in the temperature evolution. The definition of s in the horizontal axis can be found in Equations (7) and (8) for the left and right panels, respectively. For both of the detonations, the hot spots have a density of $\sim 2 \times 10^7 \text{ g cm}^{-3}$ and size of $\sim 10^2 \text{ km}$. These conditions are sufficient to generate CO detonation according to S09. Thus, these CO detonations appropriately emerge. These hot spots are also resolved in our simulations. In these densities ($\sim 2 \times 10^7 \text{ g cm}^{-3}$), the space resolutions are $\sim 13 \text{ km}$ for both the hot spots, according to Equation (1) in Section 2.

As described above, we do not overproduce any He and CO detonations. However, we may possibly miss the initiation of detonation. In other words, we may fail to follow the initiation of He and CO detonations from hot spots, even if the hot spots satisfy the conditions of H13 and S09. Moreover, H13 and S09 have just shown sufficient conditions for He and CO detonations, respectively. Fisher et al. (2019) have shown that a turbulent environment generates He and CO detonations more easily than predicted by H13 and S09. Nevertheless, we do not miss the initiation of detonations for all the models with respect to the conditions of H13 and S09. Moreover, turbulence is not effective in our setup, since we do not follow mass transfer phases. In summary, we do not overproduce or miss any detonations in our simulations.

Appendix B Propagation of Detonation

In this appendix we investigate detonation speeds and jumps in density and temperature due to the detonations. First, we show He detonations in CO60He00, He45R09, and CO90He54, and next CO detonations in CO60He00 and CO90He54.

Figure 17 shows the He detonation in the primary WD of CO60He00. The definition of s in the horizontal axis can be found in Equation (4). The detonation speed is $\sim 1.2 \times 10^4 \text{ km s}^{-1}$ at the rest frame of fuels. Since the velocity of ashes is $\sim 5 \times 10^3 \text{ km s}^{-1}$ at the rest frame of fuels, the ash velocity is $\sim 7 \times 10^3 \text{ km s}^{-1}$ at the rest frame of the detonation, which is comparable to the sound velocity of ashes. Thus, the detonation speed is consistent with the Chapman–Jouguet (CJ) speed. The density jump is also consistent with the CJ detonation as follows. In the strong limit of the CJ detonation, the density ratio of the ash to the fuel should be $(\gamma_{\text{ash}} + 1)/\gamma_{\text{ash}}$ according to Equation (129.15) of Landau & Lifshitz (1959), where γ_{ash} is the adiabatic index of the ash. Since the ash pressure is dominated by radiation pressure, $\gamma_{\text{ash}} = 4/3$. Thus, the density ratio should be $\lesssim 2$. The ash temperature is $\lesssim 3 \times 10^9 \text{ K}$ for the fuel density with $7 \times 10^5 \text{ g cm}^{-3}$. This is compatible with the ash temperature with $\gtrsim 3 \times 10^9 \text{ K}$ for the fuel density with 10^6 g cm^{-3} in H13.

Figure 18 shows the He detonation in the companion WD of He45R09. The definition of s is described in Equation (5). We find that the detonation speed is consistent with the CJ speed, taking into account the ash velocity and the ash sound velocity. Similarly to the He detonation in CO60He00, the density jump is also consistent with that in the strong limit of the CJ detonation. The ash temperature is $\sim 3 \times 10^9 \text{ K}$ for the fuel density of $\sim 10^6 \text{ g cm}^{-3}$. This is in good agreement with H13's results.

Figure 19 shows the He detonation in the companion WD of CO90He54. The horizontal axis s is expressed in Equation (6). The detonation speed is $\sim 1.0 \times 10^4 \text{ km s}^{-1}$, consistent with the CJ speed. The density jump is also consistent with that in the strong limit of the CJ detonation. The ash temperature is $\sim 2 \times 10^9 \text{ K}$ for the fuel density of $< 6 \times 10^5 \text{ g cm}^{-3}$. This is compatible with H13's results.

Figure 20 shows the CO detonations in the primary WD of CO60He00 and in the companion WD of CO90He54. The

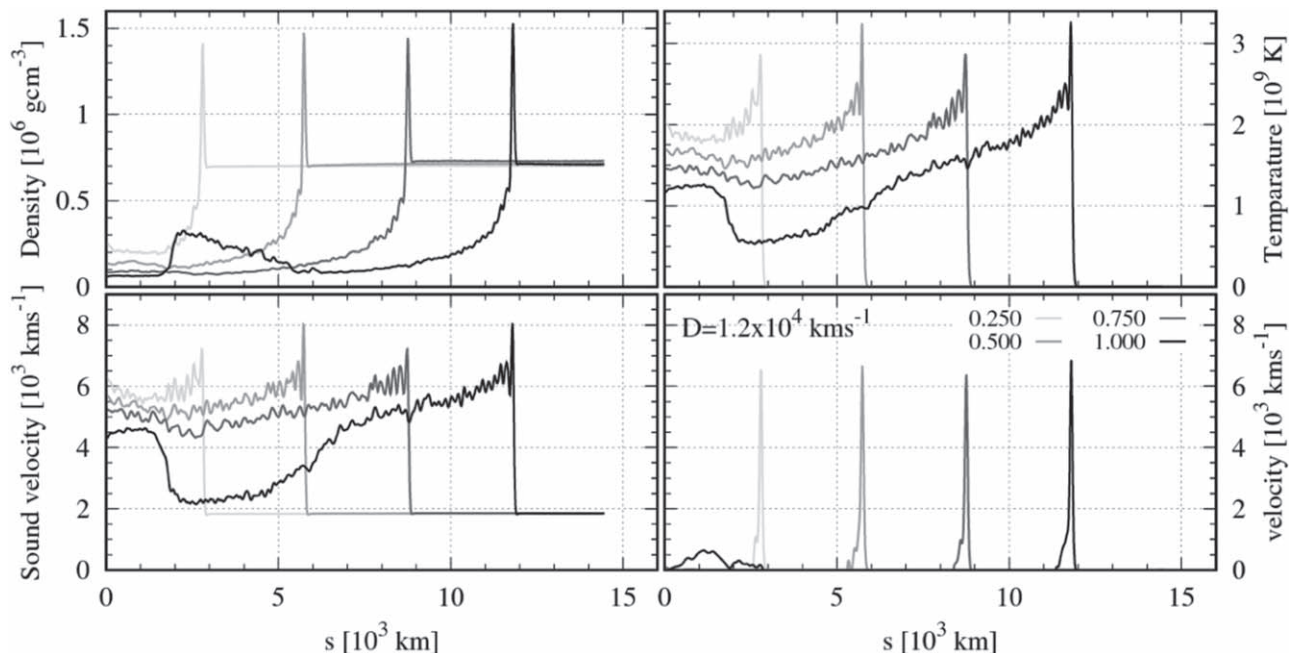


Figure 17. He-detonation profiles in the primary WD for CO60He00. Density, temperature, sound velocity, and velocity at the rest frame of the center of the primary WD are shown from $t = 0.25 \text{ s}$ to $t = 1 \text{ s}$. D indicates the detonation speed relative to the fuel materials.

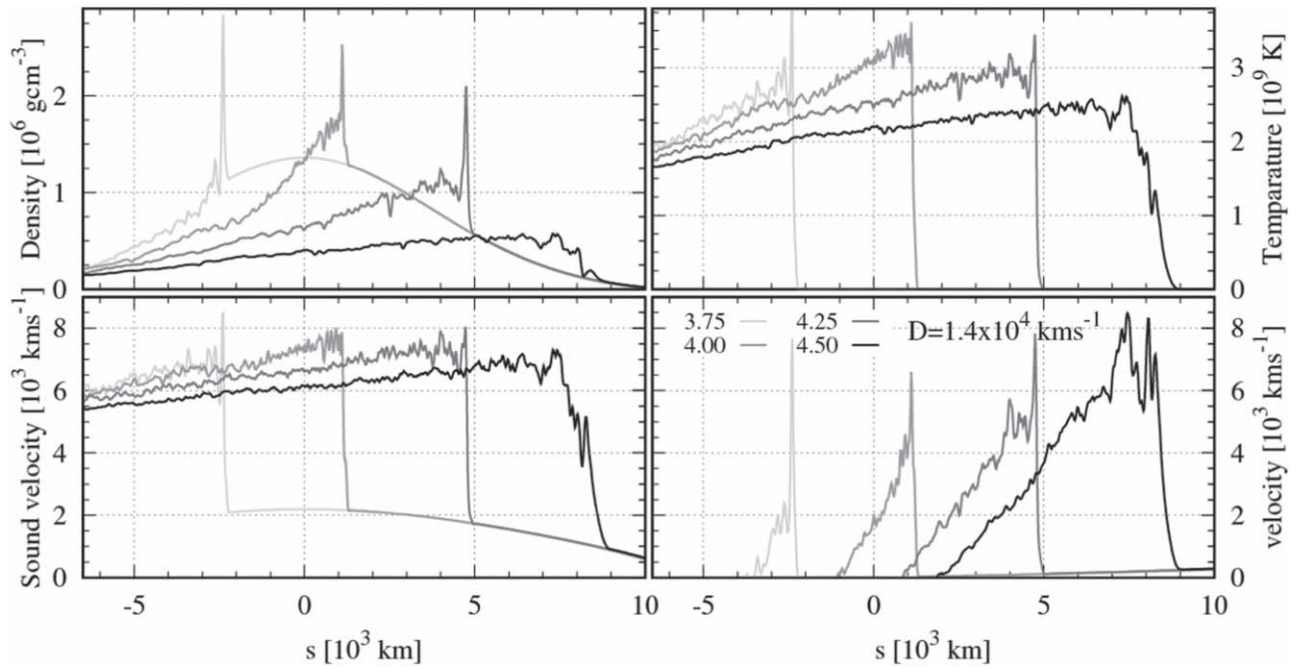


Figure 18. He-detonation profiles in the companion WD for He45R09. Density, temperature, sound velocity, and velocity at the rest frame of the center of the companion WD are shown from $t = 3.75$ s to $t = 4.5$ s. D indicates the detonation speed relative to the fuel materials.

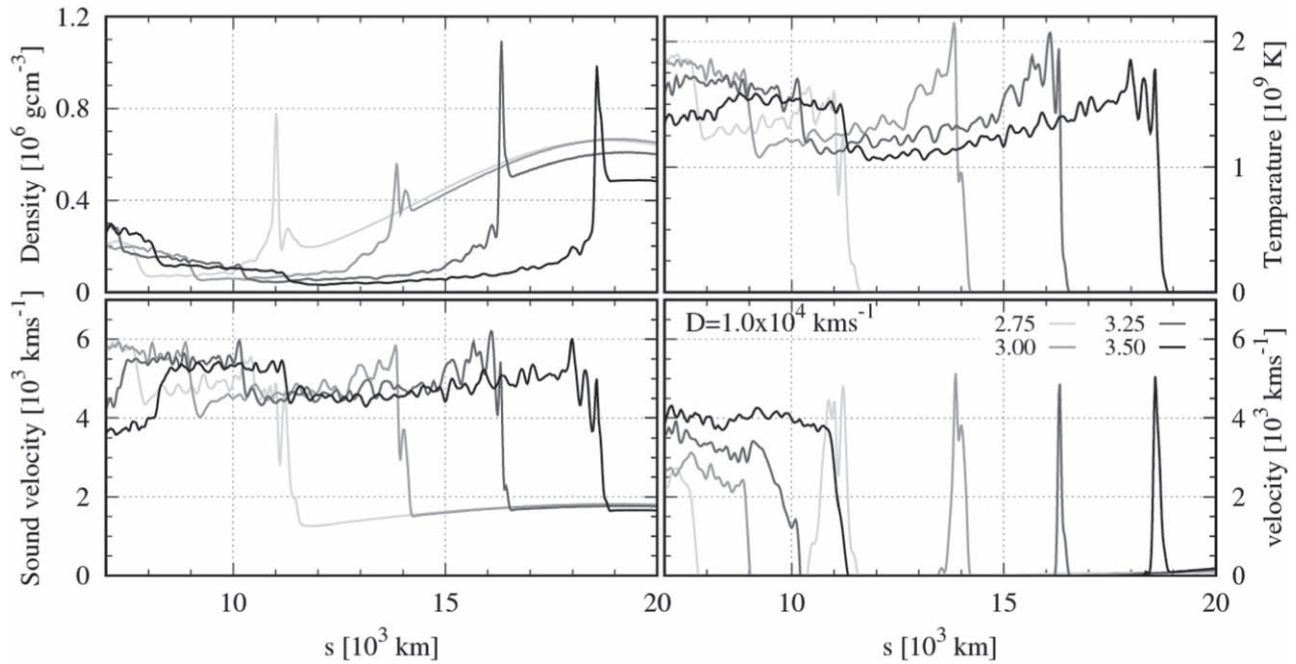


Figure 19. He-detonation profiles in the companion WD for CO90He54. Density, temperature, sound velocity, and velocity at the rest frame of the center of the companion WD are shown from $t = 2.75$ s to $t = 3.5$ s. D indicates the detonation speed relative to the fuel materials.

definitions of s in the left and right panels are the same as in the left and right panels of Figure 16, respectively. Since the fuel density exceeds $2 \times 10^7 \text{ g cm}^{-3}$ for both the CO detonations, these detonations should be a so-called pathological type of detonation (Khokhlov 1989). According to Gamezo et al. (1999), such detonations have a speed of $\sim 1.2 \times 10^4 \text{ km s}^{-1}$

when the fuel density is $(2\text{--}3) \times 10^7 \text{ g cm}^{-3}$. This is consistent with the CO detonations in our models. Moreover, Sharpe (1999) has shown that the ash density and temperature are, respectively, $\sim 7 \times 10^7 \text{ g cm}^{-3}$ and $6 \times 10^9 \text{ K}$ in the fuel density of $\sim 4 \times 10^7 \text{ g cm}^{-3}$. This is in good agreement with the CO detonation at $t = 1.75$ s in CO60He00.

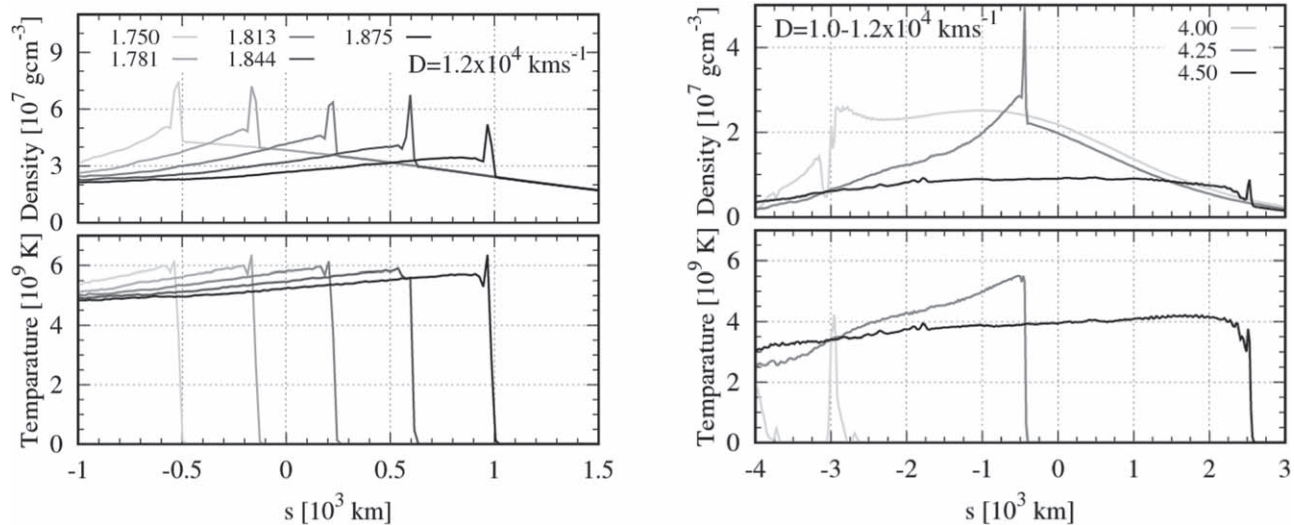


Figure 20. CO detonations in the primary WD of CO60He00 (left) and in the companion WD of CO90He54 (right). D indicates the detonation speed relative to the fuel materials.

ORCID iDs

Ataru Tanikawa <https://orcid.org/0000-0002-8461-5517>
 Ken'ichi Nomoto <https://orcid.org/0000-0001-9553-0685>
 Naohito Nakasato <https://orcid.org/0000-0003-1195-5710>
 Keiichi Maeda <https://orcid.org/0000-0003-2611-7269>

References

- Benvenuto, O. G., Panei, J. A., Nomoto, K., Kitamura, H., & Hachisu, I. 2015, *ApJL*, 809, L6
- Cartier, R., Hamuy, M., Pignata, G., et al. 2014, *ApJ*, 789, 89
- Chayer, P., Fontaine, G., & Wesemael, F. 1995a, *ApJS*, 99, 189
- Chayer, P., Vennes, S., Pradhan, A. K., et al. 1995b, *ApJ*, 454, 429
- Dave, P., Kashyap, R., Fisher, R., et al. 2017, *ApJ*, 841, 58
- De, K., Kasliwal, M. M., Polin, A., et al. 2019, *ApJ*, 873, 18
- Dehnen, W., & Aly, H. 2012, *MNRAS*, 425, 1068
- Di Stefano, R., Voss, R., & Claeys, J. S. W. 2011, *ApJL*, 738, L1
- Dilday, B., Howell, D. A., Cenko, S. B., et al. 2012, *Sci*, 337, 942
- Dong, S., Katz, B., Kollmeier, J. A., et al. 2018, *MNRAS*, 479, L70
- Dong, S., Katz, B., Kushnir, D., & Prieto, J. L. 2015, *MNRAS*, 454, L61
- Dupuis, J., Fontaine, G., Pelletier, C., & Wesemael, F. 1992, *ApJS*, 82, 505
- Eggleton, P. P. 1983, *ApJ*, 268, 368
- Fenn, D., Plewa, T., & Gawryszczak, A. 2016, *MNRAS*, 462, 2486
- Fink, M., Röpke, F. K., Hillebrandt, W., et al. 2010, *A&A*, 514, A53
- Fisher, R., Mozumdar, P., & Casabona, G. 2019, *ApJ*, 876, 64
- Folatelli, G., Phillips, M. M., Morrell, N., et al. 2012, *ApJ*, 745, 74
- Fryxell, B., Olson, K., Ricker, P., et al. 2000, *ApJS*, 131, 273
- Fryxell, B., Olson, K., Ricker, P., et al. 2010, FLASH: Adaptive Mesh Hydrodynamics Code for Modeling Astrophysical Thermonuclear Flashes, Astrophysics Source Code Library, ascl:1010.082
- Gamezo, V. N., Wheeler, J. C., Khokhlov, A. M., & Oran, E. S. 1999, *ApJ*, 512, 827
- Guillochon, J., Dan, M., Ramirez-Ruiz, E., & Rosswog, S. 2010, *ApJL*, 709, L64
- Hachisu, I., Kato, M., & Nomoto, K. 2012, *ApJL*, 756, L4
- Hamers, A. S., Pols, O. R., Claeys, J. S. W., & Nelemans, G. 2013, *MNRAS*, 430, 2262
- Hillebrandt, W., Kromer, M., Röpke, F. K., & Ruitter, A. J. 2013, *FrPhy*, 8, 116
- Hirai, R., Sawai, H., & Yamada, S. 2014, *ApJ*, 792, 66
- Hitomi Collaboration, Aharonian, F., Akamatsu, H., et al. 2017, *Natur*, 551, 478
- Holcomb, C., Guillochon, J., De Colle, F., & Ramirez-Ruiz, E. 2013, *ApJ*, 771, 14
- Hosseinzadeh, G., Sand, D. J., Valenti, S., et al. 2017, *ApJL*, 845, L11
- Hoyle, F., & Fowler, W. A. 1960, *ApJ*, 132, 565
- Hsiao, E. Y., Burns, C. R., Contreras, C., et al. 2015, *A&A*, 578, A9
- Iben, I., Jr., Nomoto, K., Tornambe, A., & Tutukov, A. V. 1987, *ApJ*, 317, 717
- Iben, I., Jr., & Tutukov, A. V. 1984, *ApJS*, 54, 335
- Iben, I., Jr., & Tutukov, A. V. 1985, *ApJS*, 58, 661
- Iben, I., Jr., & Tutukov, A. V. 1991, *ApJ*, 370, 615
- Iwasawa, M., Tanikawa, A., Hosono, N., et al. 2016, *PASJ*, 68, 54
- Jiang, J.-A., Doi, M., Maeda, K., et al. 2017, *Natur*, 550, 80
- Jiang, J.-a., Doi, M., Maeda, K., & Shigeyama, T. 2018, *ApJ*, 865, 149
- Justham, S. 2011, *ApJL*, 730, L34
- Kashyap, R., Fisher, R., García-Berro, E., et al. 2015, *ApJL*, 800, L7
- Kashyap, R., Fisher, R., García-Berro, E., et al. 2017, *ApJ*, 840, 16
- Kawai, Y., Saio, H., & Nomoto, K. 1988, *ApJ*, 328, 207
- Kelly, P. L., Fox, O. D., Filippenko, A. V., et al. 2014, *ApJ*, 790, 3
- Khokhlov, A. M. 1989, *MNRAS*, 239, 785
- Kromer, M., Fremling, C., Pakmor, R., et al. 2016, *MNRAS*, 459, 4428
- Landau, L. D., & Lifshitz, E. M. 1959, Fluid Mechanics (Oxford: Pergamon Press)
- Leung, S.-C., & Nomoto, K. 2018, *ApJ*, 861, 143
- Li, W., Bloom, J. S., Podsiadlowski, P., et al. 2011, *Natur*, 480, 348
- Litke, K. C., Chu, Y.-H., Holmes, A., et al. 2017, *ApJ*, 837, 111
- Livne, E. 1990, *ApJL*, 354, L53
- Livne, E., & Glasner, A. S. 1990, *ApJ*, 361, 244
- Lorén-Aguilar, P., Isern, J., & García-Berro, E. 2010, *MNRAS*, 406, 2749
- Maeda, K., Jiang, J.-a., Shigeyama, T., & Doi, M. 2018, *ApJ*, 861, 78
- Maeda, K., & Terada, Y. 2016, *IMPD*, 25, 1630024
- Maoz, D., Hallakoun, N., & Badenes, C. 2018, *MNRAS*, 476, 2584
- Maoz, D., Mannucci, F., & Nelemans, G. 2014, *ARA&A*, 52, 107
- McWilliam, A., Piro, A. L., Badenes, C., & Bravo, E. 2018, *ApJ*, 857, 97
- Nomoto, K. 1982, *ApJ*, 257, 780
- Nomoto, K., Thielemann, F.-K., & Yokoi, K. 1984, *ApJ*, 286, 644
- Pakmor, R., Kromer, M., Röpke, F. K., et al. 2010, *Natur*, 463, 61
- Pakmor, R., Kromer, M., Taubenberger, S., & Springel, V. 2013, *ApJL*, 770, L8
- Papish, O., Soker, N., García-Berro, E., & Aznar-Siguán, G. 2015, *MNRAS*, 449, 942
- Paquette, C., Pelletier, C., Fontaine, G., & Michaud, G. 1986, *ApJS*, 61, 197
- Raskin, C., Timmes, F. X., Scannapieco, E., Diehl, S., & Fryer, C. 2009, *MNRAS*, 399, L156
- Rosswog, S., Kasen, D., Guillochon, J., & Ramirez-Ruiz, E. 2009, *ApJL*, 705, L128
- Sato, Y., Nakasato, N., Tanikawa, A., et al. 2015, *ApJ*, 807, 105
- Sato, Y., Nakasato, N., Tanikawa, A., et al. 2016, *ApJ*, 821, 67
- Schaefer, B. E., & Pagnotta, A. 2012, *Natur*, 481, 164
- Seitenzahl, I. R., Meakin, C. A., Townsley, D. M., Lamb, D. Q., & Truran, J. W. 2009, *ApJ*, 696, 515
- Sharpe, G. J. 1999, *MNRAS*, 310, 1039
- Shen, K. J., Boubert, D., Gänsicke, B. T., et al. 2018a, *ApJ*, 865, 15
- Shen, K. J., Kasen, D., Miles, B. J., & Townsley, D. M. 2018b, *ApJ*, 854, 52
- Shen, K. J., & Moore, K. 2014, *ApJ*, 797, 46
- Shen, S., & Schwab, J. 2017, *ApJ*, 834, 180
- Silverman, J. M., & Filippenko, A. V. 2012, *MNRAS*, 425, 1917
- Stritzinger, M. D., Shappee, B. J., Piro, A. L., et al. 2018, *ApJL*, 864, L35

- Tanikawa, A. 2018a, [ApJ](#), 858, 26
- Tanikawa, A. 2018b, [MNRAS](#), 475, L67
- Tanikawa, A., Nomoto, K., & Nakasato, N. 2018, [ApJ](#), 868, 90
- Tanikawa, A., Sato, Y., Nomoto, K., et al. 2017, [ApJ](#), 839, 81
- Tanikawa, A., Yoshikawa, K., Nitadori, K., & Okamoto, T. 2013, [NewA](#), 19, 74
- Tanikawa, A., Yoshikawa, K., Okamoto, T., & Nitadori, K. 2012, [NewA](#), 17, 82
- Taubenberger, S., Kromer, M., Pakmor, R., et al. 2013, [ApJL](#), 775, L43
- Timmes, F. X. 1999, [ApJS](#), 124, 241
- Timmes, F. X., Hoffman, R. D., & Woosley, S. E. 2000, [ApJS](#), 129, 377
- Timmes, F. X., & Swesty, F. D. 2000, [ApJS](#), 126, 501
- Toonen, S., Perets, H. B., & Hamers, A. S. 2018, [A&A](#), 610, A22
- van Rossum, D. R., Kashyap, R., Fisher, R., et al. 2016, [ApJ](#), 827, 128
- Webbink, R. F. 1984, [ApJ](#), 277, 355
- Wendland, H. 1995, [Advances in Computational Mathematics](#), 4, 389
- Wheeler, J. C., Lecar, M., & McKee, C. F. 1975, [ApJ](#), 200, 145
- Whelan, J., & Iben, I., Jr. 1973, [ApJ](#), 186, 1007
- Woosley, S. E., & Kasen, D. 2011, [ApJ](#), 734, 38
- Woosley, S. E., Taam, R. E., & Weaver, T. A. 1986, [ApJ](#), 301, 601
- Yamaguchi, H., Badenes, C., Foster, A. R., et al. 2015, [ApJL](#), 801, L31
- Yamanaka, M., Kawabata, K. S., Kinugasa, K., et al. 2009, [ApJ](#), 707, L118
- Yamanaka, M., Maeda, K., Tanaka, M., et al. 2016, [PASJ](#), 68, 68
- Zenati, Y., Toonen, S., & Perets, H. B. 2019, [MNRAS](#), 482, 1135